RESEARCH PAPER

Effect of Topology on Transient Dynamic and Shock Response of Polymeric Lattice Structures

J. S. Weeks[1] · G. Ravichandran[1,2]

Abstract

Architected cellular materials, such as lattice structures, offer potential for tunable mechanical properties for dynamic applications of energy absorption and impact mitigation. In this work, the static and dynamic behavior of polymeric lattice structures was investigated through experiments on octet-truss, Kelvin, and cubic topologies with relative densities around 8%. Dynamic testing was conducted via direct impact experiments (25–70 m/s) with high-speed imaging coupled with digital image correlation and a polycarbonate Hopkinson pressure bar. Mechanical properties such as elastic wave speed, deformation modes, failure properties, particle velocities, and stress histories were extracted from experimental results. At low impact velocities, a transient dynamic response was observed which was composed of a compaction front initiating at the impact surface and additional deformation bands whose characteristics matched low strain-rate behavior. For higher impact velocities, shock analysis was carried out using compaction wave velocity and Eulerian Rankine–Hugoniot jump conditions with parameters determined from full-field measurements.

Keywords Lattice structure · Transient dynamic · Shock · Compaction · Failure · Digital image correlation

Introduction

The crushing deformation of cellular materials at low internal stresses makes them desirable for dynamic applications of energy absorption and impact mitigation [1]. Lattice structures are a class of architected cellular materials that consist of a periodic arrangement of similar unit cells with structural components such as rods, plates, or sheets [2–4]. These materials may be considered across two lengths scales dependent upon the characteristic length of a lattice member: the unit cell (UC) structural length scale, or the bulk material length scale where the lattice is treated as a continuum. Technological advances in additive manufacturing (AM) have greatly expanded the design space of these materials due to high feature resolution, fast manufacturing speeds, and large build volumes, and as a result, a large variety of materials may be manufactured across nanometer to centimeter length scales [4–6]. Access to this design space allows engineering of tunable mechanical properties of lattice structures through varying geometry and base material. Many geometric variations of lattice structures have been realized using structural components such as rods [3], plates [7], smooth surfaces [8], hollow struts [9], or with unique unit cell designs from bio-inspired [10] and topology-optimization [11] techniques.

Lattice structures may be characterized by relative density (ratio of density of the lattice material to density of the parent material), unit cell topology (shape), and base material. Lattice structures exhibit behavior consistent with their base materials such as plasticity [12, 13] and heat treatment effects [14] in metals, brittle fracture in ceramics or glassy materials [15–18], and large deformations in elastomers [19, 20]. Lattice structure geometry is defined by relative density (also recognized as volume fraction of actual material) and unit cell topology which affect mechanical properties such as relative stiffness, relative failure strength, and deformation modes [3, 21]. Rod-based geometries may be characterized as "stretching-dominated" where lattice deformation occurs due to tensile or compressive loads along lattice members

✉ J. S. Weeks
  jweeks@caltech.edu

  G. Ravichandran
  ravi@caltech.edu

[1] Division of Engineering and Applied Science, California Institute of Technology, Pasadena, CA 91125, USA

[2] Jio Institute, Ulwe, Navi Mumbai, Maharashtra 410206, India

or "bending-dominated" where deformation occurs from bending of lattice members. This characterization may be defined using structural analysis and Maxwell's stability criterion generalized to three dimensions [22, 23] and supports modeling of rod-based lattices as pin-jointed rods and structures. Due to their structural rigidity, "stretching-dominated" geometries are expected to have up to three times higher stiffness than "bending-dominated" geometries at a relative density of 10% [24]. These deformation behaviors provide a classification technique for lattice structures and indicate effective geometries to explore and compare across the design space.

Lattice structures show varied mechanical response under dynamic loading, similar to other cellular materials [25]. Under high strain-rate (> 1000 s^{-1}) loading, lattices have demonstrated material effects such as strain-rate strengthening in metallic materials [21, 26, 27] and strain-rate stiffening in polymeric materials [28]. Deformation modes in this regime are similar to those of low strain-rate loading and collapse typically initiates in the middle of the lattice specimen. Under impact loading (> 250 m/s), a compaction front develops and propagates from the impact surface of the lattice and has been demonstrated experimentally in polymeric [29, 30] and metallic lattices [31, 32]. This compaction 'wave' has been modeled as a *shock* in cellular materials such as wood [33], honeycombs [34, 35], and foams [36–39] as well as in metallic lattice structures [32]. This shock response may be modeled using 1D uniaxial planar shock theory and considering the compaction wave front as a density discontinuity in the material. At lower impact velocities, a transient dynamic response has also been demonstrated in honeycombs [35] and foams [38]. Under these loading conditions, deformation does not propagate as discontinuities in density in the form of compaction and instead additional deformation bands form within the cellular material. This behavior may also be expected in lattice structures, but no prior studies have experimentally investigated such response and the transition to the shock regime. Another relatively less explored topic is the effect of topology (geometry of the UC) on transient dynamic response and transition to shock-like behavior.

Typical planar shock experiments use laser interferometry to measure particle velocities on a surface of a target material [40, 41] which is used to quantify the bulk shock response in the form of a shock velocity-particle velocity equation of state. Laser interferometry has been successfully applied to shock experiments on periodic cellular materials [42], but does not capture details of the material deformation which may exist at the UC length scale. Full-field measurements are necessary to characterize the response of lattice structures and cellular materials due to inhomogenous deformation. Techniques such as X-ray phase contrast imaging [43] have been used to study lattice structure shock behavior [29–31] and while these techniques are effective in understanding the volumetric response, they require powerful X-rays at advanced facilities such as synchrotrons, are limited in measurement quantity (frames/images), and specimens exist typically at smaller length scales [$\mathcal{O}$ (mm)]. Digital image correlation (DIC) [44] has emerged as a powerful technique in experimental mechanics which allows for full-field displacement measurements and has been readily applied to foams [38, 45] and lattice structures [26, 32, 46]. While DIC is limited to surface measurements, it offers high measurement quantity (number of images) based upon state-of-the-art camera capabilities and requires simpler experimental set-ups; these advantages make DIC an excellent experimental technique to study shock behavior of cellular materials.

In this work, the transient dynamic and shock response of polymeric lattice structures and the effect of topology was explored through direct impact experiments. High-speed imaging and digital image correlation were used to extract full-field measurements of kinematics during impact loading of lattice specimens and the deformation modes and mechanical response were analyzed. The low strain-rate, transient dynamic, and shock behavior of Kelvin (KEL), octet-truss (OT), and cubic (CUB) topologies were investigated. These topologies were chosen due to having rod-based architectures with distinct mechanical behaviors: Kelvin lattices demonstrate "bending-dominated" behavior [3, 28], octet-truss lattices demonstrate "stretching-dominated" behavior [47], and cubic lattices were chosen as a simple geometry with struts oriented along loading direction.

Section "Materials and Methods" describes the experimental methods of this work through specimen design and characterization and description of low strain-rate and direct impact experimental techniques. Section "Results and Discussion" then presents the experimental results and discussion of the low strain-rate, compaction, and shock behavior of lattice structures with different topologies. Finally, section "Summary and Conclusions" presents the summary and conclusions of this work.

Materials and Methods

Design and Manufacture of Polymeric Lattice Structures

Lattice structure specimens were designed using cubic, Kelvin, and octet-truss unit cells with rod-based struts and a target relative density (volume fraction), ρ^*/ρ_s, of 10% (Fig. 1). A low relative density was chosen such that topologies showed distinct behavior. At higher relative densities, lattice structure deformation is typically yield-dominated and behavior for various topologies may appear similar.
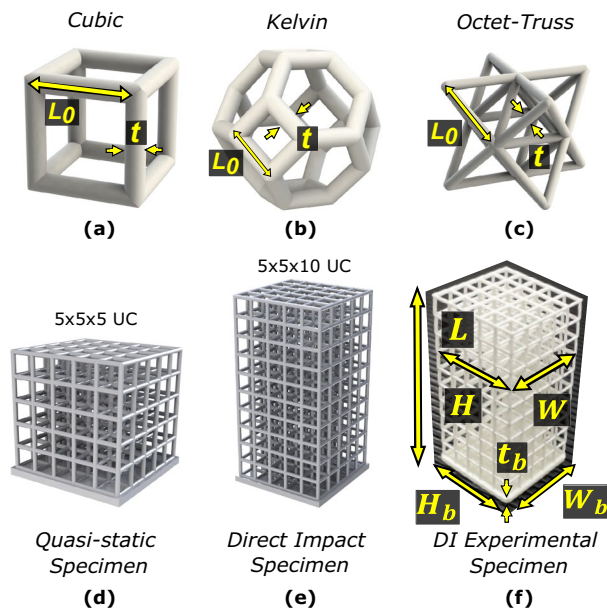
Fig. 1 **a** Cubic, **b** Kelvin, and **c** octet-truss unit cell geometries with characteristic length, L_0, and strut thickness, t; and cubic topology with **d** CAD $5 \times 5 \times 5$ UC geometry, **e** CAD $5 \times 5 \times 10$ UC geometry, and **f** experimental $5 \times 5 \times 10$ UC specimen with relevant dimensions

Table 1 CAD dimensions for characteristic length, L_0, and strut thickness, t, for cubic, Kelvin, and octet-truss unit cell geometries

Topology	L_0 [mm]	t [mm]
Cubic	4.80	0.935
Kelvin	1.70	0.625
Octet-Truss	3.40	0.440

For example, the octet-truss topology transitions from a buckling-dominated response to yield-dominated response around relative densities of 30% [21].

Unit cell geometries were created in SolidWorks (Dassualt Systemes, Providence, RI) with characteristic length, L_0, and strut thickness, t, as shown in Fig. 1. Two types of specimen were designed for each topology with a $5 \times 5 \times 5$ unit cell (UC) geometry used for low strain-rate testing and a $5 \times 5 \times 10$ UC geometry used for direct impact testing. L_0 was chosen for each topology to produce a unit cell width of 4.8 mm and the strut thickness was chosen to match a relative density of computed-aided design (CAD) $5 \times 5 \times 10$ specimens to 10%. Values used in specimen design are shown in Table 1. Baseplates were also added to improve manufacturability and help ensure planar loading; a 25 mm square baseplate with 1.5 mm thickness was used for octet-truss and Kelvin specimens and a 26 mm square baseplate with 1.5 mm thickness was used for cubic specimens.

Lattice structures were additively manufactured using a vat polymerization technique with Digital Light Processing (DLP) technology. The layer-by-layer projection manufacturing technique of DLP allows for faster printing compared

to point-based stereolithography techniques and permits a self-supporting build direction along the length of the specimen. An Autodesk Ember DLP 3D printer (San Rafael, CA) with a 405 nm wavelength light and 2.8 s exposure time per 25 µm layer was used with Colorado Photopolymer Solutions (Boulder, CO) PR57-W photoresin. After printing, specimens were rinsed in an isopropyl alcohol bath and allowed to dry for at least 3 h before testing.

Relative density was calculated for all experimental specimens using dimensions labeled in Fig. 1f. Relative density was calculated using volume fraction measurements as follows:

$$\rho^*/\rho_s = \frac{V_{mass} - V_b}{V_f} = \frac{V_{mass} - t_b H_b W_b}{(L - t_b)HW} \quad (1)$$

where V_{mass} is the experimental volume of the full specimen found from mass measurements and assuming a constant material density, V_b is the volume of the rectangular baseplate, and V_f is the space-filling volume of the lattice. The mass density of the photopolymer was determined as 1200 kg/m³ in previous work [28]. V_b was calculated from thickness, t_b, width, W_b, and height, H_b, of the baseplate and V_f was calculated using the specimen length, L, width, W, and height, H.

Low Strain-Rate Experiments

Low strain-rate experiments were performed on $5 \times 5 \times 5$ lattice specimens using a MTS Model 358.10 servo-hyraulic actuator machine (Eden Prairie, MN) with a 13.3 kN capacity axial load cell. Preliminary experiments on $5 \times 5 \times 10$ lattice specimens demonstrated macroscopic out-of-plane bending behavior due to shear localizations and long specimen lengths. This behavior results from the structural geometry, but does not adequately describe the general behavior of a lattice defined by its topology and relative density, and therefore a $5 \times 5 \times 5$ UC configuration was chosen for low strain-rate testing. Lattice specimens were compressed at a rate of 1.5 mm/min, corresponding to a nominal strain-rate of $\dot{\epsilon} \approx 0.001 \text{ s}^{-1}$, until densification. Experimental images were taken at 24 frames per second (fps) using a Fastec IL5 High-Speed Camera (San Diego, CA) with a 100 mm Tokina AT-X Pro lens (Tokyo, Japan) and a Techniquip FOI-150-UL continuous light source (Pleasanton, CA). A speckle pattern was applied to the hydraulic crosshead and 2D digital image correlation (DIC) using Vic2D (Correlated Solutions, Columbia, SC) was conducted at 1 fps to extract displacements. A subset size of 53 pixels (px) with a step size of 5 px was used for an area of interest of 36 mm × 16 mm (8 px/mm) in the DIC analysis.

Relevant experimental dimensions and corresponding relative density for specimens used in low strain-rate

Table 2 Specimen characterization for low strain-rate experiments

Experiment #	$m[g]$	$L[mm]$	$W[mm]$	$H[mm]$	t_b [mm]	W_b [mm]	H_b [mm]	ρ^*/ρ_s[%]
CUB_{QS1}	2.723	25.784	24.480	24.518	1.676	25.766	25.788	7.987
CUB_{QS2}	2.702	25.848	24.514	24.530	1.728	25.816	25.828	7.580
CUB_{QS3}	2.573	25.936	24.560	24.568	1.608	25.826	25.840	7.298
KEL_{QS1}	2.656	25.674	24.244	24.220	1.818	24.794	24.844	7.806
KEL_{QS2}	2.758	25.788	24.290	24.230	1.927	24.768	24.826	7.929
KEL_{QS3}	2.399	24.992	24.196	24.234	1.570	24.814	24.754	7.533
OT_{QS1}	2.534	25.414	24.146	24.114	1.768	24.848	24.860	7.406
OT_{QS2}	2.473	25.222	23.962	23.866	1.772	24.824	24.796	7.236
OT_{QS3}	2.349	25.164	23.952	23.878	1.640	24.796	24.836	7.042
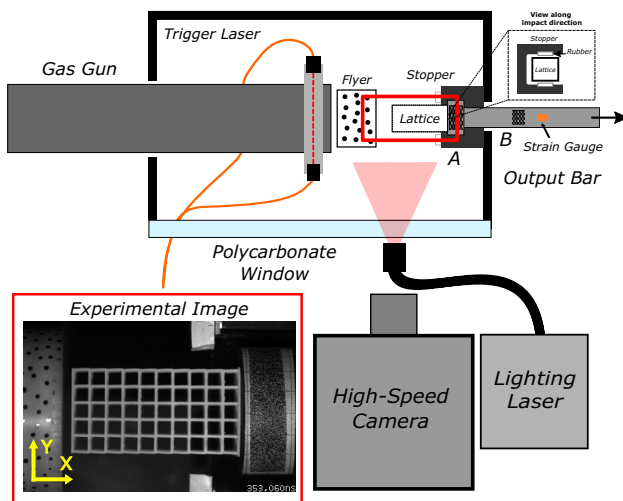
Fig. 2 Schematic of direct impact experimental set-up with high-speed imaging and polycarbonate (PC) Hopkinson pressure bar. Insert shows an experimental image of speckled Delrin flyer, cubic lattice specimen and speckled PC anvil prior to impact. *X* and *Y* are the axial (horizontal) and transverse (vertical) coordinates, respectively, in the undeformed configuration

experiments are shown in Table 2. The experimentally measured relative densities showed significantly lower values than the as-designed value of 10% which may be attributed to the in-plane (XY) manufacturing resolution (50 microns) of the Autodesk Ember DLP printer and post-manufacturing shrinkage of the photopolymer.

Direct Impact Experiments

Direct impact experiments with high-speed imaging were conducted on $5 \times 5 \times 10$ lattice specimens at impact velocities from 25 to 70 m/s using a gas gun and polycarbonate (PC) Hopkinson pressure bar (HPB) as shown in Fig. 2. A Delrin disk (flyer) with 50.80 mm diameter and 25.40 mm length was used to impact specimens inside a chamber with a transparent PC window. Lattice specimens were taped to a PC anvil (31.75 mm diameter) which in turn was press fit

onto a longer PC bar (25.40 mm diameter, 1.83 m length) and surrounded by a C-shaped aluminum stopper and two pieces of rubber. This 'stopper' prevented the flyer from fully densifying the specimen and transmitting high forces that could inelastically deform the pressure bar through high strains. The baseplate-anvil interface of each specimen was positioned such that the flyer contacted the rubber pieces and aluminum stopper before full densification of the specimen was attained and thereby much of the impact force of the flyer was transmitted to these parts rather than being fully transmitted into the polymeric output bar.

High-speed images were taken using a Hyper Vision HPV-X2 camera (Shimadzu, Kyoto, Japan) with a Nikon 70–300 mm f/4.5–5.6 G lens (Tokyo, Japan) and lighting from a non-coherent CAVILUX Smart laser (Cavitar, Tampere, Finland) with 40 ns pulse lengths. 128 images were taken at a constant framing interval (8500–22,500 ns) set to maximize number of images taken during deformation depending on target impact velocities of 30 m/s, 50 m/s, and 70 m/s. Image capture and data acquisition was triggered using a Wilcom F6230A visual fault locator (Belmont, NH) directed through the gas gun barrel using fiber optic cables, a Thorlabs PDA10A2 photodiode (Newton, NJ), and a 2.5 GHz Tektronix DPO 3014 digital oscilloscope (Beaverton, OR). A trigger was sent as the flyer interrupted the visual fault locator and a voltage drop from the photodiode was registered for longer than 100 µs. Specimen characteristics and imaging parameters for all direct impact experiments are shown in Table 3.
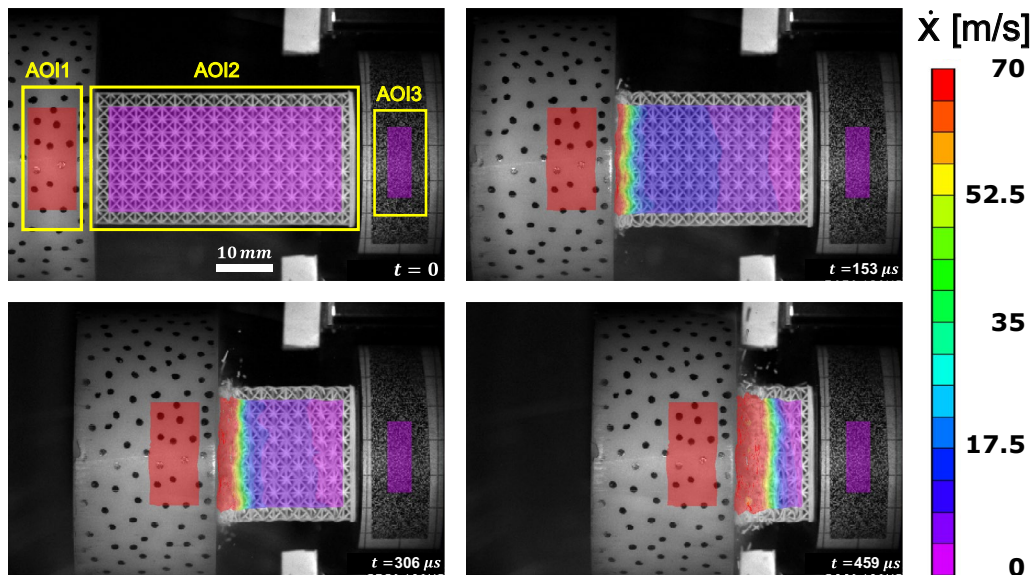
Digital Image Correlation Analysis

Digital image correlation (DIC) was performed on three areas of interest (AOI) in the experimental images. The AOIs and corresponding DIC analyses for an octet-truss lattice impacted at 73.1 m/s (Exp. #OT_{DI3}) are shown in Fig. 3.

A Sharpie pen (Fine Point) was used to create a random speckle pattern on the flyer for AOI1, black spray paint and tape were used to make the speckle pattern on the anvil for AOI3, and the lattice geometry itself served as a unique

Table 3 Specimen characterization and imaging parameters for direct impact experiments

Experiment #	$m[g]$	$L[mm]$	$W[mm]$	$H[mm]$	t_b [mm]	W_b [mm]	H_b [mm]	$\rho^*/\rho_s[\%]$	$\Delta t[\mu s]$	FPS	v_i [m/s]
CUB_{DI1}	4.191	49.594	24.552	24.550	1.703	25.834	25.784	8.171	20,000	50,000	24.21
CUB_{DI2}	4.090	49.608	24.552	24.560	1.598	25.878	25.810	8.089	12,000	83,333	49.34
CUB_{DI3}	3.806	48.810	24.650	24.660	0.840	25.936	25.880	8.942	8500	117,647	61.22
KEL_{DI1}	3.314	48.290	24.300	24.238	0.710	24.832	24.850	8.291	22,500	44,444	24.81
KEL_{DI2}	3.695	49.016	24.424	24.470	0.990	24.804	24.810	8.605	12,000	83,333	45.83
KEL_{DI3}	3.835	48.582	24.304	24.308	0.925	24.844	24.900	9.317	8,500	117,647	67.27
OT_{DI1}	3.776	49.148	24.010	24.016	1.808	24.770	24.762	7.465	22,500	44,444	25.63
OT_{DI2}	3.603	48.802	23.966	23.968	1.798	24.704	24.778	7.048	12,000	83,333	51.29
OT_{DI3}	3.041	47.304	23.728	23.800	1.070	24.798	24.780	7.186	8,500	117,647	73.11

Fig. 3 Digital image correlation analysis on Delrin flyer (AOI1), octet-truss lattice specimen (AOI2), and PC anvil (AOI3) at times t = 0, 153 µs, 306 µs, and 459 µs after impact for Exp. #OT_{DI3}. Particle velocity ($\dot{x}$) results from all AOI are superimposed on each image

subset for AOI2. A subset size of 23 px (4.6 mm) was used for AOI1 and AOI3 and a subset size of 27 px (5.4 mm) was used for AOI2 (corresponding to ∼ 1.1 of a unit cell) with a step size of 1 px used in all analyses. While local strains of the lattice are inherently smoothed during the analysis due to a subset size greater than the unit cell size, these subset sizes remain relevant to approximate the material as a continuum. Incremental correlation was used for all analyses due to large deformations of the lattice and to remain consistent across all three areas of interest. Additionally, a 0.09 px confidence error threshold was used for data removal of highly deformed or overexposed regions. Particle velocities shown in Fig. 3 were computed in Vic2D using a constant timing interval and three-point central difference numerical method. The impact velocity of the flyer, v_i, in each experiment was computed from DIC of the flyer (AOI1) prior to impact and is shown in Table 3. Anvil particle velocities

were $\mathcal{O}(10)$ mm/s and much smaller than the magnitudes of the flyer and lattice particle velocities.

Hopkinson Pressure Bar Analysis

Strain gauge measurements on the polycarbonate pressure bar allowed extraction of the force acting on the distal (non-impacted) end of the lattice through conventional Hopkinson pressure bar (HPB) analysis. Two Vishay EA-13-031CE-350/LE gauges (1/4 bridge configuration) were placed diametrically opposite 0.6 m from the lattice-anvil interface and a Vishay 2310B signal conditioning amplifier (Raleigh, NC) and Agilent MSO9404A oscilloscope (20 GSa/s sample rate) (Santa Clara, CA) were used to record strain gauge voltage data. A low input voltage of 1.4 V was used to avoid heating effects in the strain gauges. Following

elastic HPB analysis [40], the particle velocity and force at the bar interface may be found using:

$$v(t) = c_0 \epsilon_{SG}(t) \qquad (2)$$

$$F(t) = EA\epsilon_{SG}(t) \qquad (3)$$

where v is the velocity of the bar interface, E is the Young's modulus of the PC bar taken as 2.37 GPa [48], c_0 is the bulk wave speed in the PC bar taken as 1405 m/s (using $c_0 = \sqrt{E/\rho}$ with density $\rho = 1200$ kg/m^3 [48]), ϵ_{SG} is the strain-gauge measurement in the bar, F is the force experienced at the lattice-anvil interface, and A is the cross-sectional area of the bar.

Viscoelastic analysis following Bacon [49] was also carried out using an additional set of strain gauges placed 0.3 m from the lattice-anvil interface. Elastic analysis of the gauges located 0.6 m from the interface matched viscoelastic analysis evaluated at 0.6 m from the interface and typical strain measurements were also low ($\mathcal{O}(100)\mu\epsilon$) which justified the use of elastic analysis in this loading regime and experimental set-up.

Wave reflection from the end of the bar did not affect results as all strain pulse lengths were less than 1.75 ms in duration which represents the time at which wave reflection occurs at the strain gauge location.

A similar trigger was sent to imaging (high-speed camera) and HPB components (strain gauges) and allowed comparison of time-linked measurements. Velocities were extracted from both DIC and HPB analyses and used to validate strain gauge measurements. Figure 4a shows the computed anvil velocities using DIC and HPB techniques for all three topologies with an impact velocity of $\sim$ 50 m/s. The corresponding DIC location is marked as position A in Fig. 2. Velocities of $\mathcal{O}$ (0.1–0.7) m/s corresponded to subpixel resolution of the DIC analysis and the resulting DIC confidence intervals were comparable to the magnitudes of HPB measurements. Differences in HPB and DIC values may be attributed to the experimental resolution of the DIC technique and values agree within computed error bounds. An overall qualitative match in the shape and magnitude of the velocity profiles was observed.

An additional set of validation experiments was carried out at an impact velocity of $\sim$ 70 m/s with a DIC location next to the strain gauges (corresponding to position B in Fig. 2). Velocities are shown in Fig. 4b and strain measurements again showed good match with DIC measurements with differences comparable to that of anvil experiments. Qualitative matching of the velocities from both the anvil and pressure bar gives validation that strain gauge measurements are accurate and differences in measurements may be attributed to analysis techniques rather than effects of the anvil.

Results and Discussion

Low Strain-Rate Behavior of Lattice Structures

Low strain-rate experiments were performed on $5 \times 5 \times 5$ lattice specimens at a nominal strain-rate of $\dot{\epsilon} \approx 0.001 s^{-1}$. Three experiments were conducted for each topology to verify repeatability of results and specimen characteristics for each experiment are shown in Table 2. The nominal stress,
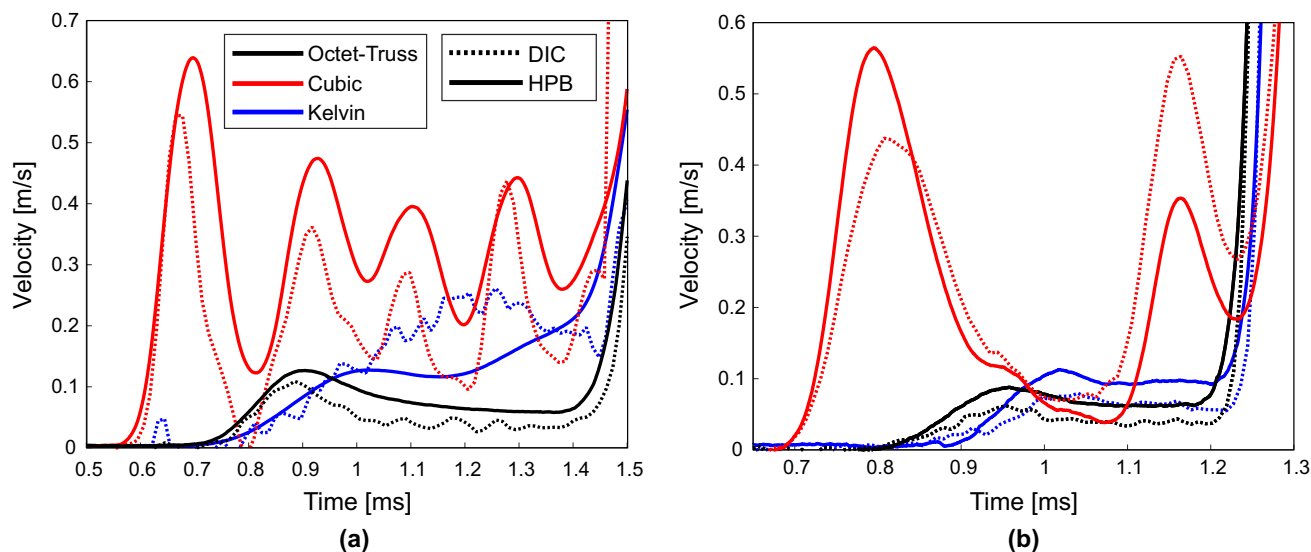

Fig. 4 Hopkinson pressure bar (HPB) measurements were validated through comparison to DIC-computed velocities of the **a** anvil at impact velocity, $v_i \approx 50$ m/s and **b** pressure bar at impact velocity, $v_i \approx 70$ m/s

σ_N, of each specimen was found by dividing load cell force measurements by the full area of the lattice ($H * W$) and the nominal strain, ϵ_N, was found by dividing DIC-computed displacements of the hydraulic crosshead by the length of the lattice ($L - t_b$). Deformation images were taken during experiments and linked in time to mechanical measurements.

Figure 5a shows the low strain-rate nominal stress-strain response (σ_N - ϵ_N) for each specimen. While variation between individual specimens exists, there is good repeatability of the general response of each topology. Specimens demonstrated behavior consistent with that of brittle cellular materials [1] which included an initial linear elastic region before a critical failure stress (σ_f) was reached and subsequent softening occurred. Then, crushing of the lattice progressed at a relatively constant plateau stress before struts began to contact and steep stiffening occurred due to densification of the material.

Images shown in Fig. 5b demonstrate the deformation modes of each lattice topology and show nominal strains of $\epsilon_N = 0, 0.1, 0.2$ and 0.6. The cubic topology showed a catastrophic failure deformation mode initiated by macroscopic buckling at strains $\epsilon_N < 0.1$ and fracture of vertical struts in a given horizontal layer of unit cells for strains $\epsilon_N > 0.1$ which then progressively failed in a layer-by-layer fashion. This behavior is demonstrated in the $\sigma_N - \epsilon_N$ response by sharp rises and drops in stress associated with the loading and failure of each layer. The octet-truss topology showed the weakest $\sigma_N - \epsilon_N$ response and deformation images revealed a buckling-dominated response which initiated after a peak failure stress. The progressive crushing of the lattice continued through buckling and showed a low, constant plateau stress until densification. This deformation mode and softening response is expected due to the "stretching-dominated"

behavior of the geometry [47]. Finally, the Kelvin topology showed a strain-hardening response with "bending-dominated" deformation concentrated at the strut nodes. This observation is consistent with Maxwell's stability criterion analysis of this geometry [24] as well as the authors' past experimental work on Kelvin lattices of the same material [28].

Low Strain-Rate Mechanical Properties

Low strain-rate mechanical deformation and failure properties were extracted from the $\sigma_N - \epsilon_N$ response of each specimen. The following properties were calculated: (1) stiffness, S, (2) specific energy absorption, E_{abs}, (3) failure stress, σ_f, and (4) failure strain, ϵ_f. S was defined through the slope of the initial $\sigma_N - \epsilon_N$ response and calculated using a linear fit of select data points ($0.01 < \epsilon_N < 0.05$) with a maximized R-squared value. E_{abs} was defined as: $E_{abs} = \frac{1}{\rho^*} \int_0^{0.6} \sigma_N d(\epsilon_N)$ where ρ^* is the mass density of the specimen and the upper integration bound of $\epsilon_N = 0.6$ was chosen to represent a typical strain before densification effects (stiffening) initiated. σ_f was defined as the maximum stress the specimen sustains before failure (softening) occurs, and ϵ_f was defined as the corresponding strain at failure.

Figure 6 shows the low strain-rate mechanical failure properties for all lattice specimens. Relative densities of the specimens were computed using Eq. (1) and showed significant distinctness in values. Particularly, the lower relative densities of the octet-truss specimens may be attributed to the smaller manufacturing dimensions of the geometry and limitations of the printer resolution.
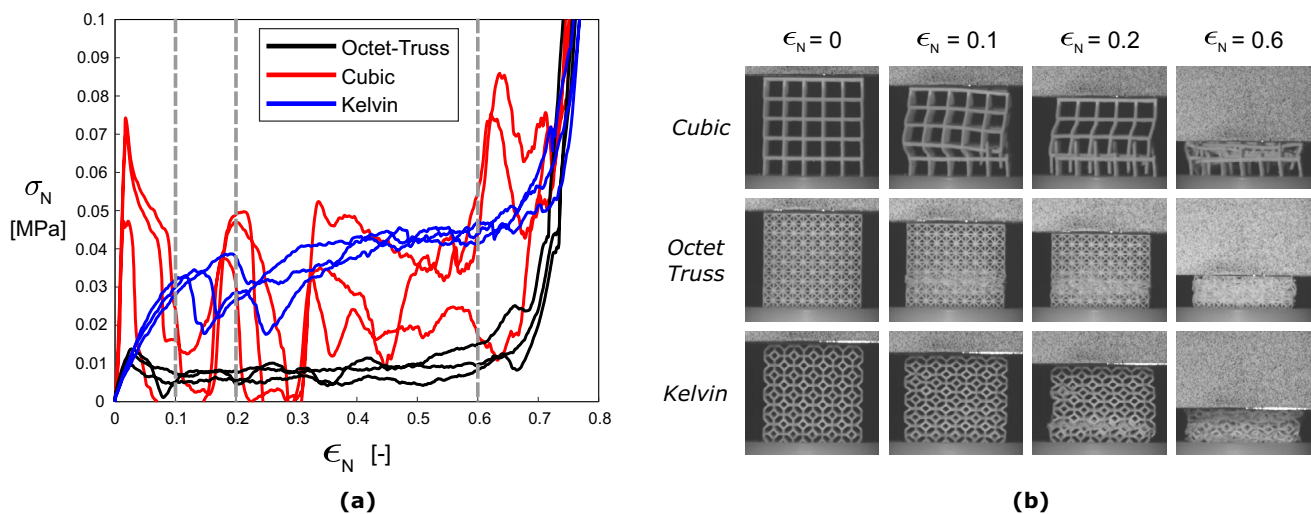

Fig. 5 Low strain-rate **a** nominal stress (σ_N)—nominal strain (ϵ_N) response and **b** deformation images of specimens at $\epsilon_N = 0, 0.1, 0.2$, and 0.6 which are represented as vertical lines in **a**
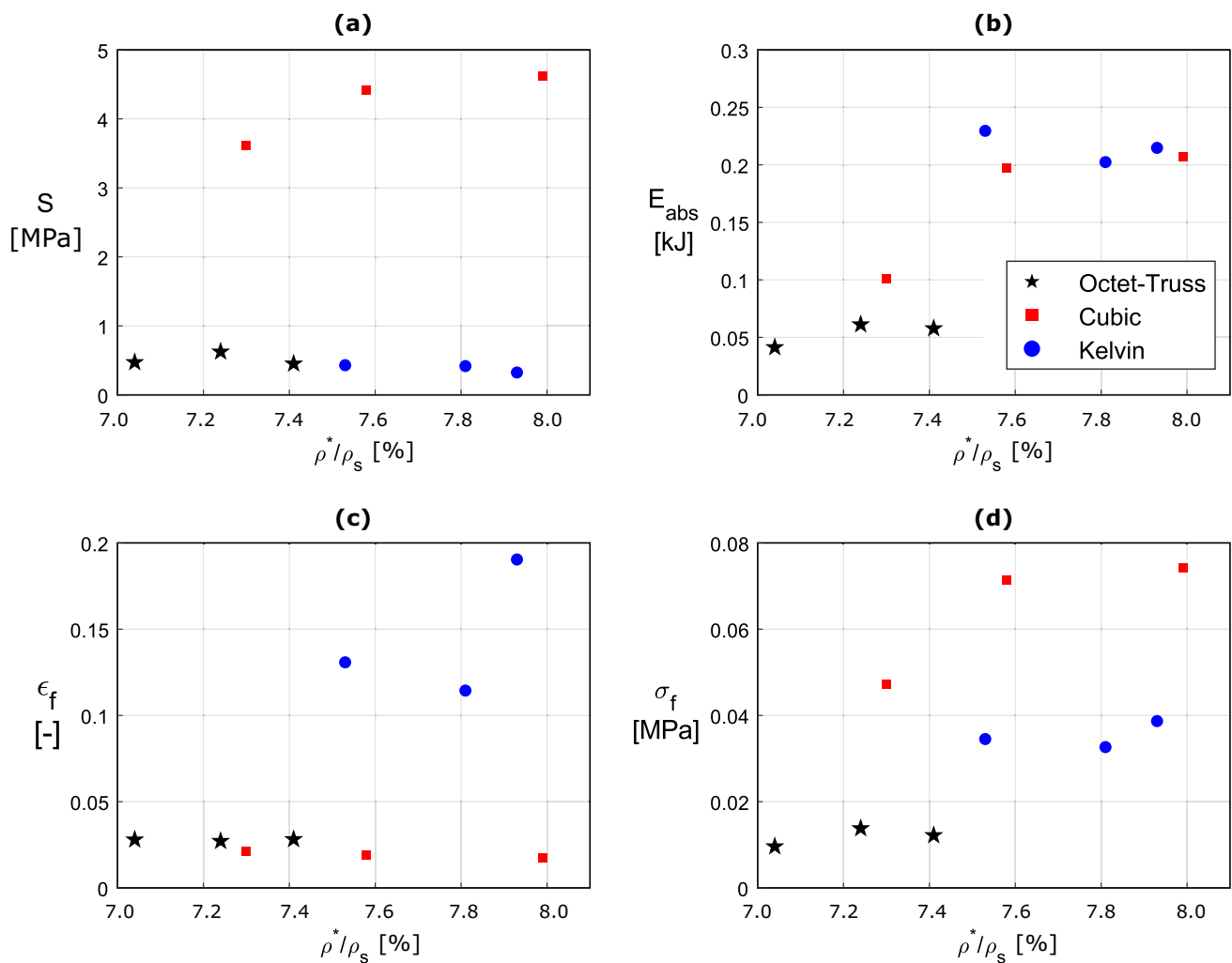
Fig. 6 Low strain-rate mechanical properties of lattice structures for **a** stiffness, S, **b** specific energy absorption, E_{abs}, **c** failure strain ϵ_f, and **d** failure stress, σ_f

Cubic specimens demonstrated the highest stiffness by a factor of ~ 5 compared to the Kelvin and octet-truss topologies. This high stiffness is in agreement with rigid "stretching-dominated" behavior which was demonstrated through an initial buckling deformation mode. Maxwell's stability criterion (as well as buckling behavior) also describes the octet-truss topology as "stretching-dominated". But, while it is expected for a "stretching-dominated" geometry to have higher stiffness than a "bending-dominated" geometry for a relative density around 10% [24], this is not apparent from experimental results for the octet-truss and Kelvin specimens. However, the stiffness of lattice structures is also dependent on relative density [3], and lower density octet-truss specimens generated slightly higher stiffness values than Kelvin specimens of higher densities. It is reasonable to conclude octet-truss lattices of similar densities would demonstrate higher values than Kelvin lattices.

The octet-truss topology showed the lowest specific energy absorption, which may be related to a buckling deformation response compared to bending (Kelvin) or fracture (cubic). Meanwhile, cubic and Kelvin topologies showed similar E_{abs} values. Considering failure properties: Kelvin specimens showed the highest failure strain while octet-truss and cubic specimens showed lower values; and cubic specimens demonstrated the greatest failure stress, followed by Kelvin, and octet-truss specimens. The failure stress results draw parallels to that of specific energy absorption and may be considered a large contributing factor to the total energy absorbed during low strain-rate loading. Densification strain was similar for all three lattice topologies with a value of ≈ 0.75 represented by convergence of the stiffening sections of the $\sigma_N - \epsilon_N$ curves in Fig. 5a. Lattice relative densities were distinct but similar in values which agrees with experimental observation of densification strain as a function of relative density in foams [1].

Elastic Wave Speeds in the Dynamic Experiments

Full-field measurements from DIC allow extraction of particle displacements over the entire impacted lattice specimens. An example of particle displacement (δ) as a function of undeformed coordinate (X) profiles for an octet-truss specimen impacted at 73.1 m/s (Exp. #OT_{DI3}) is shown in Fig. 7a. Particle displacements were computed for each undeformed horizontal coordinate (X) pixel and averaged over 20 undeformed vertical coordinate (Y) pixels about the center of the specimen, corresponding to the width across the center unit cell. Displacement—undeformed coordinate ($\delta - X$) profiles are plotted for each time instance in Fig. 7a where each line depicts data from one experimental image. Increasing time is recognized as rightward translation of each profile and positive concavity illustrates the trend of increasing displacement at all positions across the lattice.

The elastic wave front was defined using a displacement criterion of 200 μm which was chosen to approximate 1 pixel (image resolution: $\sim$ 5 pixels/mm). The DIC analysis is capable of sub-pixel accuracy and error bars are plotted, which are small ($< \pm 1.5$μm). Elastic wave speeds may then be extracted using displacement measurements since the time instance of each experimental image is known. The elastic wave front may be defined in position and time and is shown in Fig. 7b for the corresponding data in Fig. 7a. A linear fit was applied to the elastic front position-time history and the slope was taken as the wave speed. The elastic wave speed was calculated using positions $X < 35$ mm to avoid boundary effects from the baseplate and the linear trend was representative of all experiments.
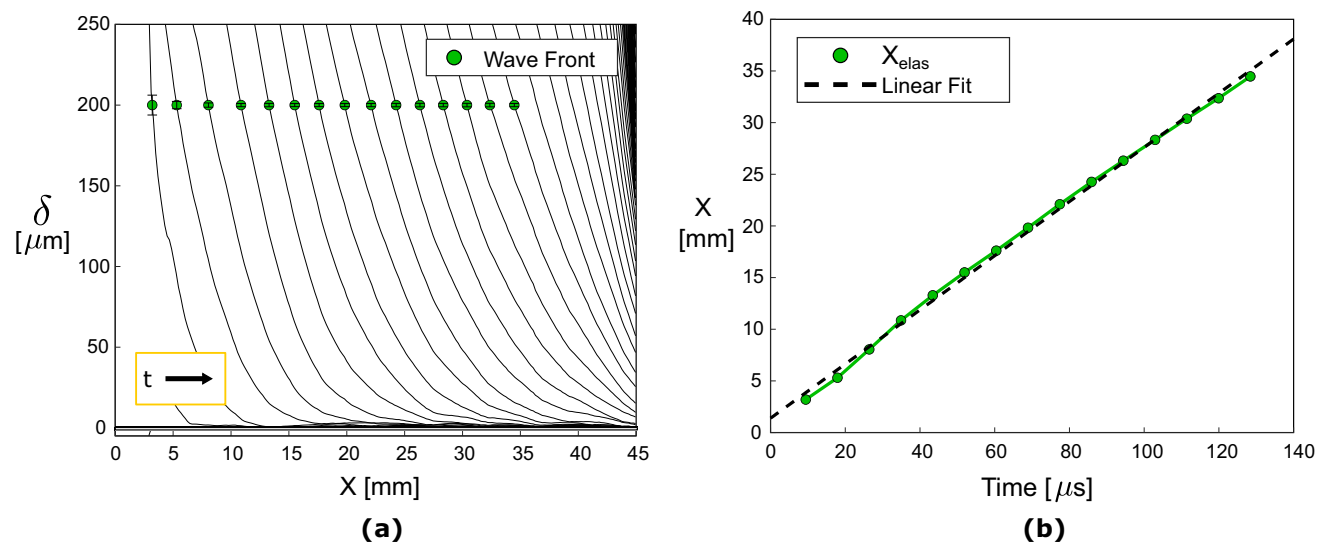
The elastic wave speeds for all impact experiments are shown in Fig. 8. Figure 8a shows the dependence of elastic wave speed on relative density. Elastic wave speeds appeared mostly constant for each topology with the cubic topology showing the highest speed followed by octet-truss and Kelvin topologies. This relationship closely follows trends of low strain-rate stiffnesses and agrees with the continuum approximation of longitudinal wave speed as $c = \sqrt{E/\rho}$ where E is Young's modulus (stiffness) of lattice specimens and density is similar for all specimens.

Figure 8b shows the dependence of elastic wave speed on impact velocity. A slight increase in elastic wave speed with impact velocity was observed for octet-truss and Kelvin topologies, while no clear trend was discernible for the cubic topology. Large confidence bounds for the cubic specimen impacted at 24.2 m/s (Exp. #CUB_{DI1}) were a result of applying a fit to few data points (due to a high wave speed and low framing rates). Though, a general increase in wave speed with impact velocity may be realized in the data and may be interpreted as a material effect by considering strain-rate stiffening of the base photopolymer material which has been observed by the authors in previous work [28].

Elastic wave speeds serve as effective properties to compare from various models and measurements of lattice structures. The elastic wave speed of the lattice, c^*, may be approximated using $c^* = \sqrt{E^*/\rho^*}$ where E^* and ρ^* are the stiffness and density of the lattice specimen, respectively. This technique along with Bloch-wave theory approximations of the stiffness has been used to find good agreement between elastic wave speeds in finite element analyses of metallic octet-truss lattice structures in previous work by the authors [32]. In this study, this relationship is used to
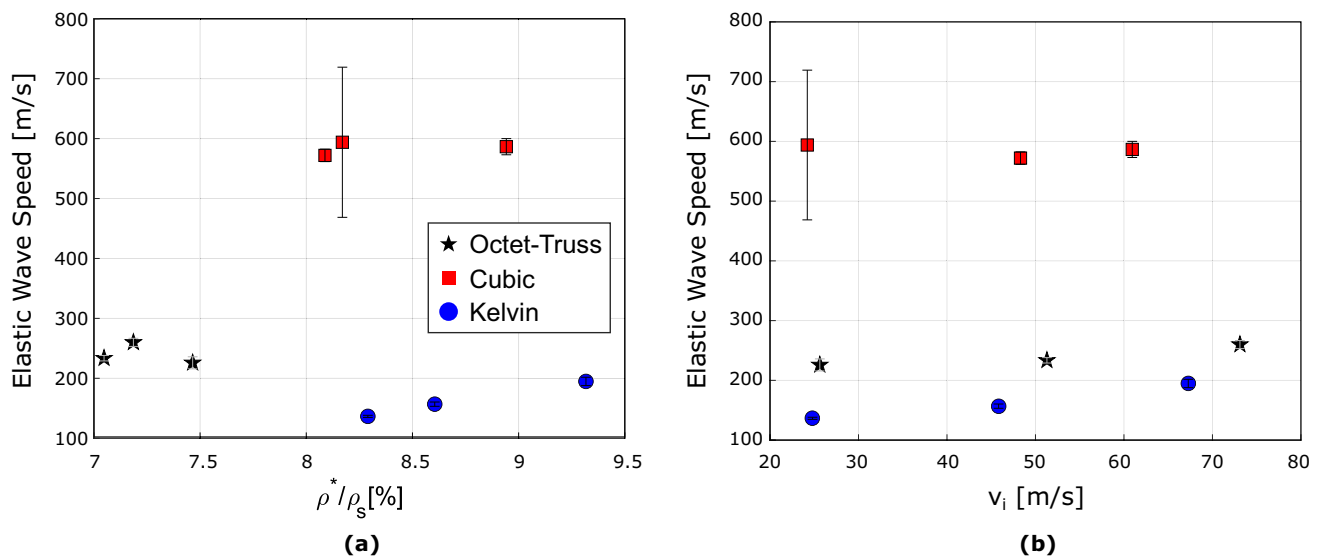

Fig. 7 **a** Particle displacement (δ)—undeformed coordinate (X) profiles with elastic wave front positions at 200 μm and **b** corresponding elastic wave front-time history for Exp. #OT_{DI3}

Fig. 8 Elastic wave speeds vs. **a** relative density, ρ^*/ρ_s, and **b** impact velocity, v_i, for cubic, Kelvin, and octet-truss specimens. Error was defined using a 95% confidence bound and was large when few data points were used for fitting

estimate the elastic wave speed of octet-truss specimens with an average value of 76.94 m/s compared to the experimentally measured average elastic wave speed of 239.78 m/s. Values differ by a factor of 3.12 which closely follows results for strain-rate stiffening trends in the base photopolymer material which demonstrates factors of about 3.5–4 [28]. It is assumed this difference is due to strain-rate (viscoelastic) material effects of the photopolymer.

Models for the octet-truss geometry have been developed and may be used to relate the elastic wave speed to base material properties [50, 51]. Messner et al. [50] have used Bloch-wave theory and a contiuum model to calculate the longitudinal elastic wave speed as $c_l = 0.707c_{bar}$ in the long wavelength limit. Using quasi-static values of $E_s = 400$ MPa, $\rho_s = 1200$ kg/m^3 for the photopolymer [28] and $c_{bar} = \sqrt{E_s/\rho_s}$, the resultant computed wave speed is 408.19 m/s. Messner [51] has also modeled the octet-truss through homogenization of the unit cell response assuming a periodic arrangement of pin-joined nodes, which produces an elastic modulus of $E^* = 0.0081E_s$ for a relative density of 7.5% and a resultant wave speed of 190 m/s. There is significant discrepancy between model-computed values and experimentally-measured wave speeds in this study. These differences may arise from consideration of an infinite lattice in the models compared to a $5 \times 5 \times 10$ finite lattice of this study, as well as local material viscoelastic or strain-rate effects of the photopolymer.

Compaction Behavior of Lattice Specimens

Deformation bands or strain concentrations occurring in different regions of cellular materials may be used to define

unique deformation regimes. Transient dynamic behavior has been observed computationally in impact loading of honeycombs of $\rho^*/\rho_s = 10\%$ at $v_i = 10$ m/s [35] and experimentally in aluminum 6061 foams of $\rho^*/\rho_s \approx 8\%$ at $v_i \approx 35$ m/s [38]. This type of behavior demonstrates deformation occurring at distal ends (honeycomb) or mid-sections (foam) in addition to deformation at the impacted surface. In contrast, a more uniform dynamic response was found at strain-rates around 1000 s^{-1} (corresponding to $v_i \approx 15$–20 m/s) in Kelvin lattice structures of $\rho^*/\rho_s = 15 - 30\%$ made from the same photopolymer used in this work. These materials demonstrated deformation bands in the middle of the specimen similar to their low strain-rate behavior [28]. During high velocity impact (e.g. $v_i > 250$ m/s) lattice structures exhibit another deformation mechanism–that of a sole progressing compaction (crushing) front initiating at the impact surface [29–32]. There exists a transition point between these deformation regimes dependent on the material, but this transition has not yet been fully explored in lattices. Impact velocities of 25–70 m/s span a range of strain-rates in between the transient dynamic and shock regimes for polymeric lattice structures investigated in this study. The mechanical response of lattice specimens was analyzed in these regimes using DIC based full-field strain and particle velocity measurements and HPB force measurements.

Deformation Modes

Deformation modes of each specimen were analyzed from full-field DIC measurements. As previously described for particle displacements in Sect. 3.2, similarly, data for each X-position pixel was averaged over the central 20 Y-position

pixels of the lattice AOI where 20 pixels was approximately the width of one UC.

Figure 9 shows deformation mode results for the octet-truss topology. Figure 9a–c show the longitudinal Lagrangian strain (ϵ_{XX})—undeformed coordinate (X) profiles for octet-truss specimens with impact velocities (v_i) of 25.6 m/s, 51.3 m/s, and 73.1 m/s, respectively. Figure 9d–f show corresponding strain-fields taken at nominal impact strains ($\varepsilon = \Delta x_{flyer}/(L - t_b)$) of 0, 0.2, 0.4, and 0.6. The $\epsilon_{XX} - X$ profiles of the time instances at these nominal impact strains are represented using bold lines in Fig. 9a–c.

For $v_i = 25.6$ m/s, Fig. 9d shows the initial development of a compaction front at $\varepsilon = 0.2$ and formation of additional deformation bands ahead of the compaction front by $\varepsilon = 0.4$. These bands may be realized through the shape of the $\epsilon_{XX} - X$ profiles in Fig 9a. Figure 9b, e show results for $v_i = 51.3$ m/s and similarly show the initial development of a compaction front from $\varepsilon = 0 - 0.4$ and an additional deformation band forming by $\varepsilon = 0.6$. Figure 9c, f show results for $v_i = 73.1$ m/s with a clearly propagating compaction front and a slight region of deformation ahead of the deformation front at $\varepsilon = 0.6$. As impact velocity increased, the prominence of the compaction front increased while that of the additional deformation band decreased. The deformation mechanism of these bands matched the low strain-rate behavior via a buckling response. In contrast, deformation at the compaction front demonstrated more crushing-like behavior.
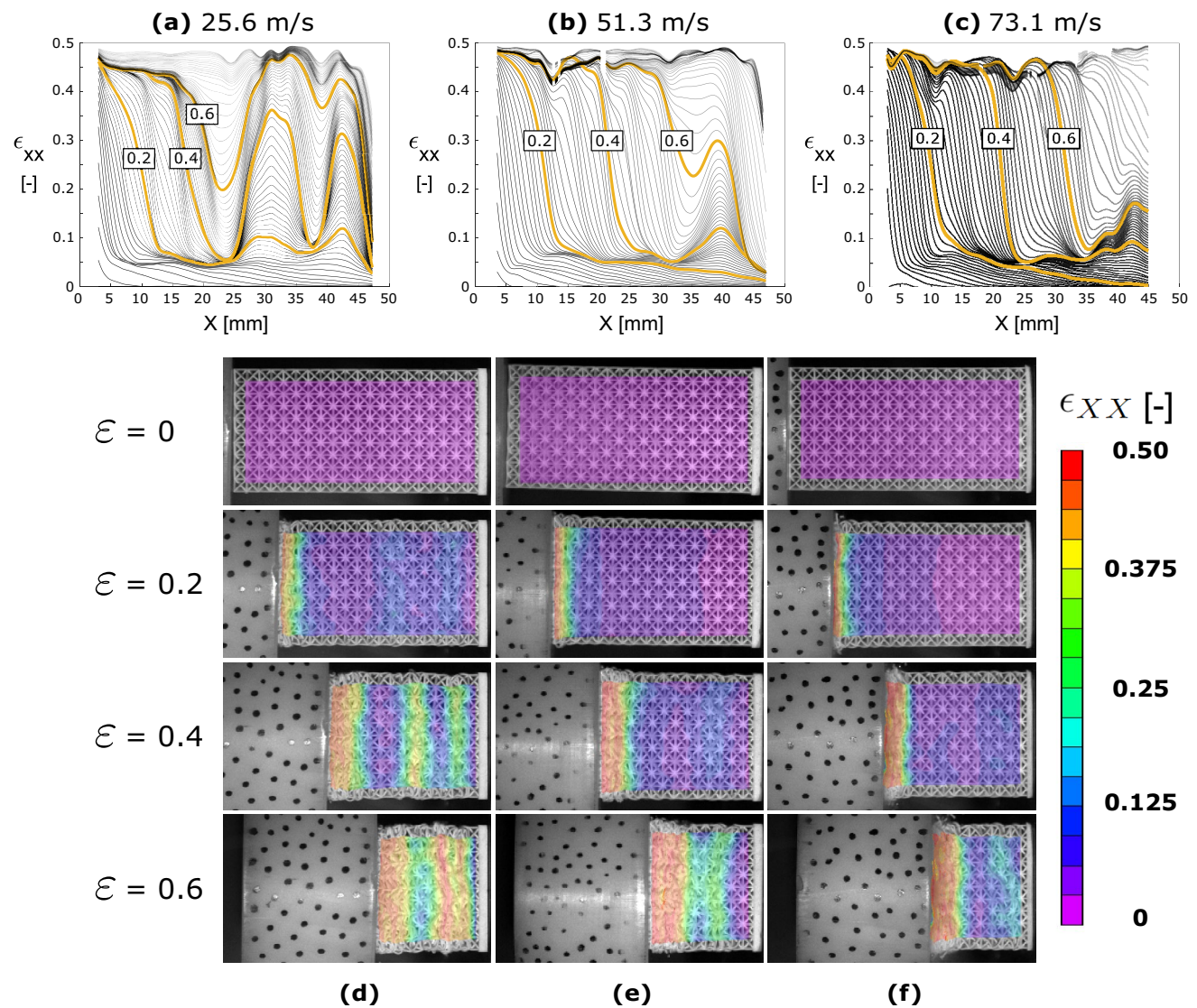

Fig. 9 Deformation modes of octet-truss topology. Lagrangian strain (ϵ_{XX})—undeformed coordinate (X) profiles for impact velocity v_i of **a** 25.6 m/s, **b** 51.3 m/s, and **c** 73.1 m/s. Corresponding strain-fields at nominal impact strains of $\varepsilon = 0, 0.2, 0.4$, and 0.6 for v_i of **d** 25.6 m/s, **e** 51.3 m/s, and **f** 73.1 m/s. Line transparency is increased at later time instances to improve data visualization

Figure 10 shows the $\epsilon_{XX} - X$ profiles and deformation images taken at $\epsilon = 0, 0.2, 0.4, 0.6$ for Kelvin lattice specimens impacted at 24.8, 45.8, and 67.3 m/s. For all impact velocities, a compaction front developed and became increasingly prominent as impact velocity increased. The $\epsilon_{XX} - X$ profiles in Fig. 10a show lines that appear to decrease somewhat linearly. This behavior is more representative of a 'transient dynamic' response than a 'shock' response which will be discussed in Sect. 3.4. The compaction wave also appears to dissipate in all experiments, represented by non-zero strains ahead of the front. Deformation ahead of the compaction front is visualized in deformation images in Fig. 10d–f and shows consistent

"bending-dominated" behavior which was observed in the low strain-rate response.

Figure 11 shows the ϵ_{XX}—X profiles and deformation images taken at $\epsilon = 0, 0.2, 0.4,$ and 0.6 for cubic lattice specimens impacted at 24.2, 49.3, and 61.2 m/s. For $v_i = 24.2$ m/s, Fig. 11a, d show deformation first initiates at the impact surface and secondly initiates near the distal-most unit cell by $\epsilon = 0.2$. Compaction then occurs at both these locations similar to what is expected in a low strain-rate response. Figure 11b, c and e, f show deformation modes for v_i of 49.3 m/s and 61.2 m/s, respectively. Unlike at $v_i = 49.3$ m/s (Exp. #CUB_{DI2}) deformation ahead of the front exists and strut fracture was observed at $v_i = 61.2$ m/s (Exp. #CUB_{DI3}). This may have resulted from manufacturing or geometric
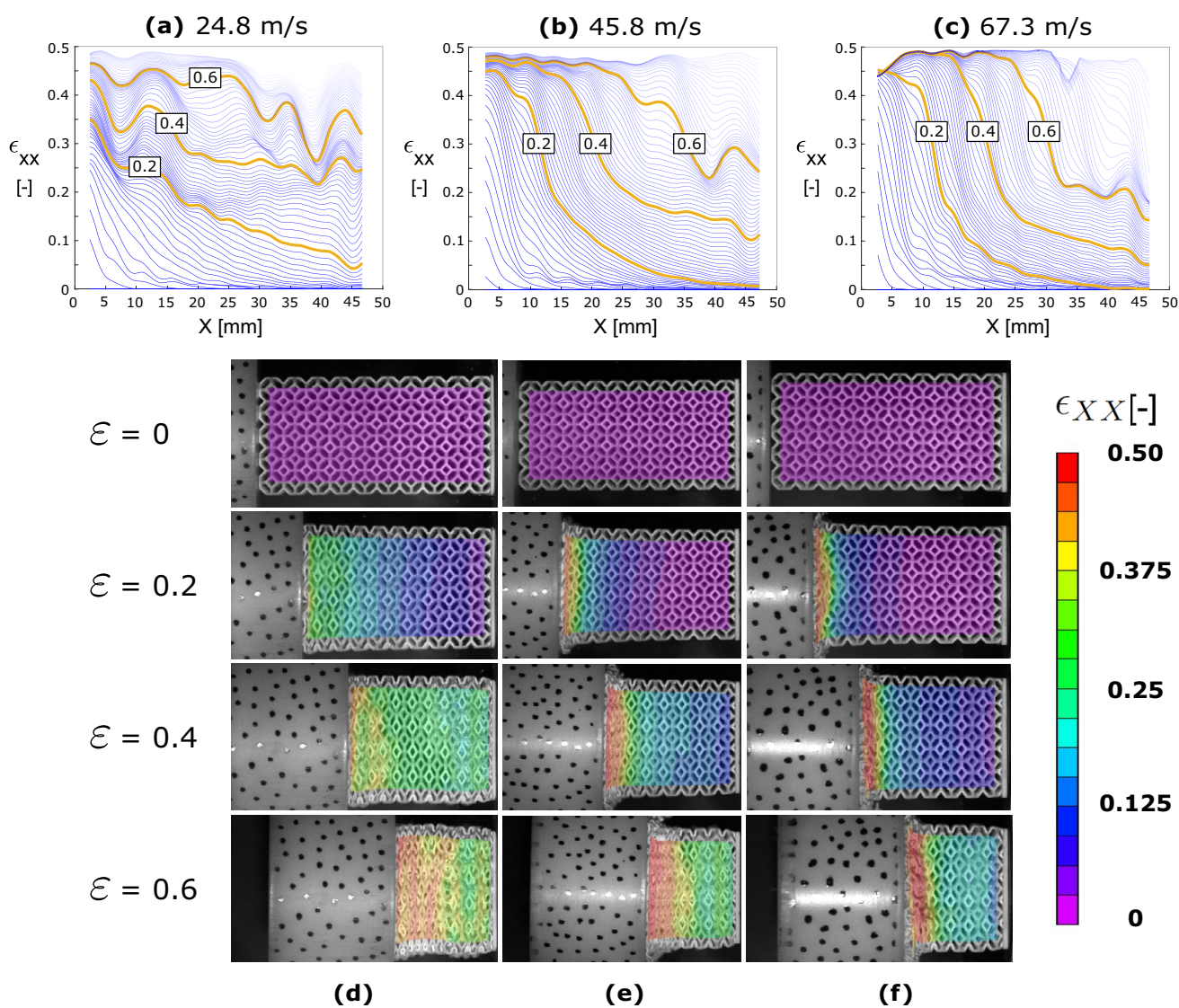

Fig. 10 Deformation modes of Kelvin topology. Lagrangian strain (ϵ_{XX})—undeformed coordinate (X) profiles for impact velocity v_i of **a** 24.8 m/s, **b** 45.8 m/s, and **c** 67.3 m/s. Corresponding strain-fields at nominal impact strains of $\epsilon = 0, 0.2, 0.4,$ and 0.6 for v_i of **d** 24.8 m/s, **e** 45.8 m/s, and **f** 67.3 m/s. Line transparency is increased at later time instances to improve data visualization
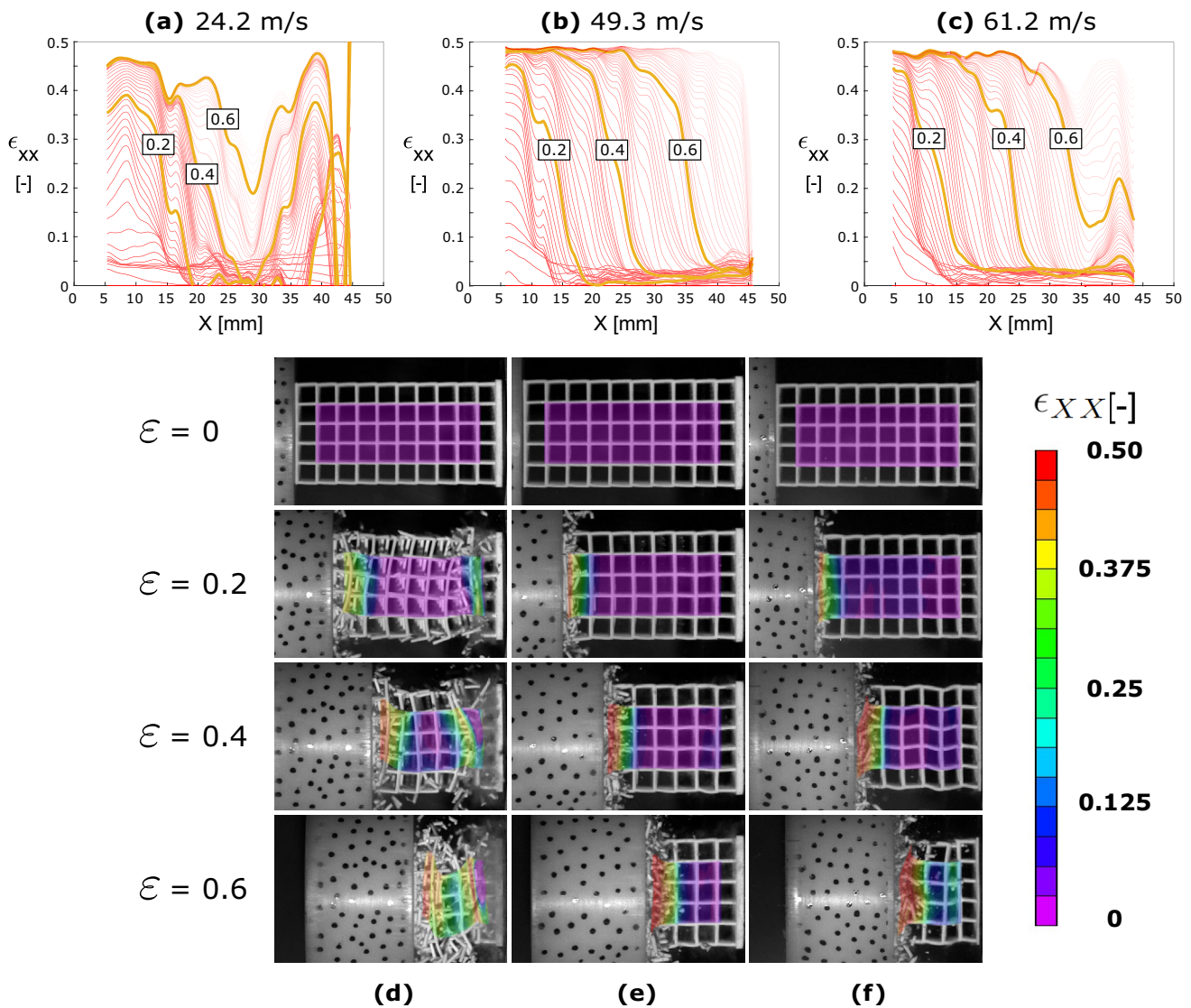
Fig. 11 Deformation modes of cubic topology. Lagrangian strain (ϵ_{XX})—undeformed coordinate (X) profiles for impact velocity v_i of **a** 24.2 m/s, **b** 49.3 m/s, and **c** 61.2 m/s. Corresponding strain-fields at nominal impact strains of $\varepsilon = 0, 0.2, 0.4$, and 0.6 for v_i of **d** 24.2 m/s, **e** 49.3 m/s, and **f** 61.2 m/s. Line transparency is increased at later time instances to improve data visualization

defects or a higher relative density of the specimen (Exp. #CUB_{DI3}: 8.942% vs Exp. #CUB_{DI2}: 8.089%) and reflects the influence of structure on the deformation response. In both cases, buckling followed by brittle fracture of the struts was observed and a clear compaction front developed. As with the Kelvin and octet-truss topologies, the cubic specimen deformation modes were similar to their low strain-rate response.

Full-field strain measurements and varying impact velocities allowed for comparison of the compaction response across topologies. In all topologies, a 'transient dynamic' response occurred at the lowest impact velocity: deformation initiated at the impact surface and additional deformation bands formed ahead of the compaction front. These

bands demonstrated deformation mechanisms similar to the lattices' low strain-rate response. A 'shock' response may be generally defined using the ϵ_{XX}—X profiles. A square-wave type curve reflects a strong shock in the material with two distinct regions of uniform strain. The strongest shocks were observed at $v_i \approx 70$ m/s; impacts at $v_i \approx 50$ m/s generally induced deformation which may be realized as a weak shock with two separate regions defined with a lower sloped curve; and impacts at $v_i \approx 25$ m/s induced deformation which should be recognized as (non-shock) compaction. The strongest shocks were found in cubic specimen, followed by octet-truss, and Kelvin specimens based upon the steepness of the $\epsilon_{XX} - X$ curves. The shock response of these lattices (considering $v_i > 45$ m/s) is further analyzed in Sect. 3.4.

Some interesting observations are also noted as follows: particularly, strains ahead of the front were higher in Kelvin lattices than other topologies which suggests an increased dissipation effect in this topology; and the cubic topology did not display compaction wave behavior at $v_i \approx 25$ m/s which demonstrates a higher initiation velocity required for a compaction wave response.

Particle Velocity Profiles

Figure 12 shows particle velocities from full-field DIC measurements for each direct impact experiment. Particle velocities were plotted for each X-position at all time instances and measurements were taken as the average of 20 Y-pixels about the center of the lattice as discussed in previous sections. Each experimental curve corresponds to data from one X-pixel position and all experimental images.

Flyer velocity was calculated using DIC and plotted for each experiment. As time increased, particle velocities of the lattice specimens converged to the speed of the flyer. Sharp deceleration of the flyer sometimes resulted from hitting the 'stopper' in the experimental set-up such as for the octet-truss specimen at $v_i = 51.3$ m/s (Exp. #OT_{DI2}). Otherwise, flyer velocity appeared to gradually decrease with time due to energy dissipation through deformation of the lattice. Convergence of the lattice particle velocities to the flyer speed has also been demonstrated in metallic lattice specimens [32] and illustrates a 'structural shock' behavior.

Particle velocities in cubic specimens appeared to exceed that of the flyer which may be attributed to the catastrophic failure mode of the topology and high kinetic energy of the failed struts. Particle velocities in cubic specimen also appeared to take longer to converge to the flyer speed than Kelvin or octet-truss specimens, which represents a longer time for compaction initiation.
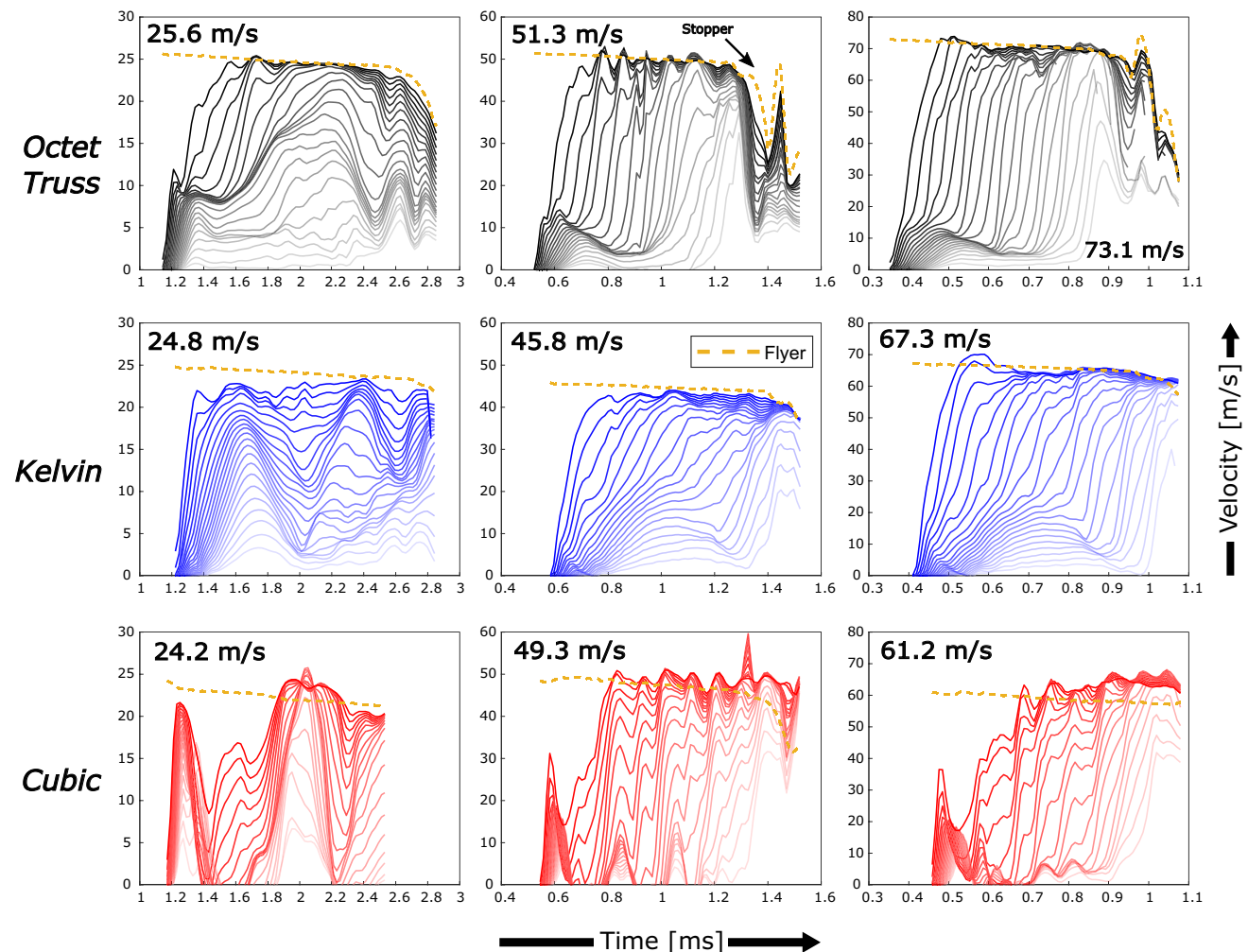

Fig. 12 Particle velocities of lattice specimens and flyers during direct impact experiments with initial impact velocity shown. Line transparency is increased for larger X-positions to improve data visualization

Sharper (smaller rise times) velocity profiles illustrate a stronger shock response apparent in experiments at higher impact velocities. Particle velocity profiles showed a precursor wave that decayed before the compaction wave arrived. This pre-cursor wave is related to the elastic wave and plastic response of the lattice specimen and corresponding particle velocities appear to follow trends of low strain-rate behavior shown in Fig. 5a. Cubic specimens showed a steep profile and large drop in value before the compaction shock arrived which is similar to the catastrophic failure mode observed at low strain-rates. Similarly, Kelvin specimens showed hardening-like profiles and octet-truss specimens showed softening-like profiles resembling the low strain-rate stress-strain ($\sigma_N - \epsilon_N$) behavior.

Stress Histories

The force acting at the distal end of the lattice specimen may be found using Eq. (3) and strain measurements (ϵ_{SG}) from the HPB. Figure 13 shows the nominal stress (σ_N)—nominal impact strain ($\epsilon = \Delta x_{flyer}/(L - t_b)$) response for each direct impact experiment. Due to varying time duration of experiments, nominal impact strain was used as a comparable quantity. The nominal impact strain represents travel of the flyer normalized by the length of the lattice rather than a representation of the strain field of the specimen. An artifact of this method is that due to wave transit times across the lattice specimen, higher impact velocities induce a larger nominal impact strain before the stress wave arrives at the distal end and a non-zero stress is encountered. Therefore, higher impact velocity experiments may be mistakenly interpreted as exhibiting less stiff responses.
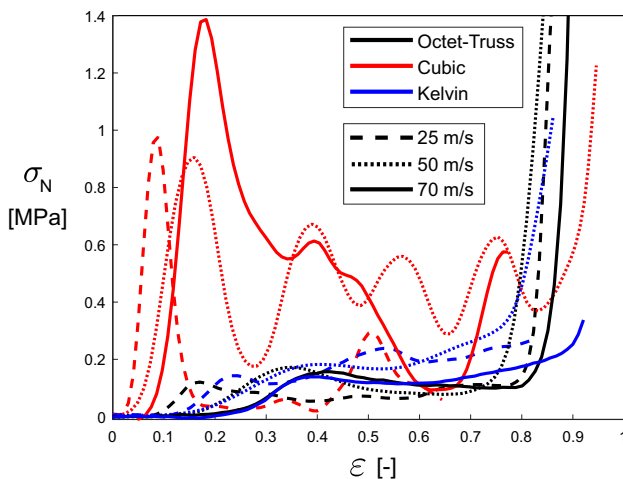

Fig. 13 Nominal stress (σ_N)—nominal impact strain (ϵ) response for lattice specimens impacted at velocities of approximately 25, 50, and 70 m/s

Across all topologies, the cubic specimens showed the stiffest and strongest response while the octet-truss and Kelvin specimens exhibited forces commensurate with each other. A slight strengthening may be realized as impact velocity increased, however, variance of force measurements may also be related to relative density of the specimens.

For each topology, force measurements from $v_i \approx 50$ m/s and $v_i \approx 70$ m/s were similar, but differed from force measurements at $v_i \approx 25$ m/s. This observation is in line with the emergence of a dominant compaction (shock) wave at these impact velocities. Overall, force measurements in these experiments resembled trends of the low strain-rate $\sigma_N - \epsilon_N$ behavior of the lattice specimens (Fig. 5a). Considering specimens with similar relative densities, results show a strain-rate strengthening factor around 15 for cubic specimens, 15 for octet-truss specimens, and 5 for Kelvin specimens.

Shock Response of Lattice Structures

While a compaction wave initiates at the impact surface of all lattice specimens in this work, it is only realized as a shock wave when it exists as the dominant deformation mechanism. This compaction front has been realized as a shock front in metallic octet-truss lattices structures under high impact velocities and the equation of state (EOS) for these materials has been defined using a linear shock velocity—particle velocity relation [32]. Properties such as density and stress behind the shock front may be found by following one-dimensional continuum shock physics theory using the notions of conservation of mass and momentum [52]. Shock jump relations following the conservation of mass and momentum are shown in Eqs. (4) and (5) as follows:

$$[\![\rho]\!]u_s = [\![\rho\dot{x}]\!] \tag{4}$$

$$[\![\rho\dot{x}]\!]u_s = [\![\rho\dot{x}^2 - \sigma]\!] \tag{5}$$

where bracket quantities $[\![q]\!]$ represent the jump value ($q^+ - q^-$) across the shock, ρ is the density, $\dot{x}$ is the Eulerian particle velocity, σ is the stress, and u_s is the shock velocity measured in the deformed or Eulerian coordinates. The Eulerian form of the jump conditions were used to account for effects of non-negligible deformation (e.g. strain, particle velocity) ahead of the shock as seen in DIC contours in Figs. 9, 10, and 11.

Parameters necessary to apply the shock jump relations were found using full-field DIC measurements. The shock front was determined by considering the particle velocity ($\dot{x}$) - undeformed (or, Lagrangian) coordinate (X) relation for each experimental image. An example of this data for the Kelvin topology impacted at 67.3 m/s (Exp. #KEL_{DI3}) is shown in Fig. 14.

Each line in Fig. 14 represents data from one experimental image. The shock front was defined as the point of maximum change in velocity for each time instance and the shock velocity was computed using a three-point central difference method on the shock front (X_s)—time (t) history. The shock front was determined for each undeformed coordinate, X, and mapped to the deformed coordinate, x, using displacement measurements, δ, such that $x = X + \delta$. Additionally, the particle velocity ahead of the shock was approximated as the point of maximum curvature ahead of the shock front position.
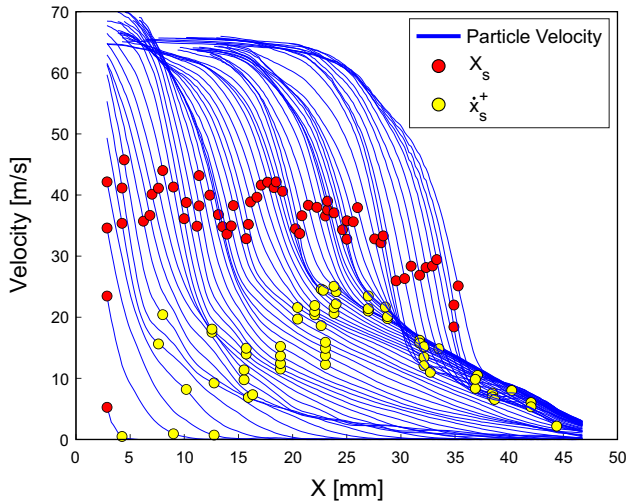
Fig. 14 Particle velocity ($\dot{x}$) vs. undeformed coordinate (X) profiles for the Kelvin topology impacted at 67.3 m/s (Exp. #KEL_{DI3}) with shock front position (X_s) and particle velocity ahead of the shock ($\dot{x}_s^+$) marked

The density ahead of the shock, ρ_s^+, was found by considering the length of the uncrushed lattice ahead of the shock. This density may be approximated by taking the ratio between the initial length of the uncrushed section of the lattice and the current length of the uncrushed section of the lattice.

$$\frac{\rho_s^+}{\rho_0} = \frac{L - t_b - X_s}{L - t_b + \delta_{anv} - x_s} \quad (6)$$

where L is the length of the full specimen, t_b is the thickness of the baseplate, δ_{anv} is the displacment of the anvil, x_s is the deformed coordinate shock front position, X_s is the undeformed coordinate shock front position, and ρ_0 is the initial density of the specimen.

The conservation of mass (Eq. 4) may be rewritten to obtain the density behind the shock (ρ^-) in terms of known parameters:

$$\rho^- = \frac{\rho^+ u_s - \rho^+ \dot{x}^+}{u_s - \dot{x}^-} \quad (7)$$

Figure 15a shows the density ahead of the compaction wave (ρ_s^+) calculated using Eq. (6) and the density behind the compaction wave (ρ_s^-) calculated using Eq. (7). The density ahead of the shock remains at a relatively constant value during deformation while the density behind the shock varies widely. Figure 14 demonstrates the particle velocity ahead of the shock ($\dot{x}_s^+$) varies widely during loading as well. The density behind the shock, ρ_s^-, is dependent on this particle velocity, $\dot{x}_s^+$, and therefore has a dependence on the lattice topology.
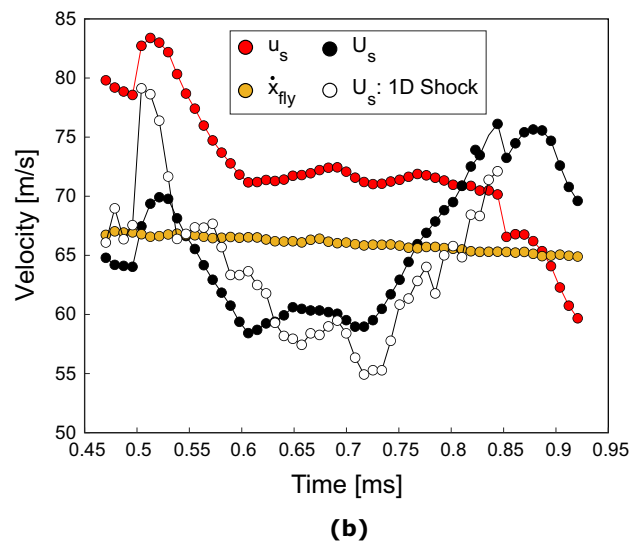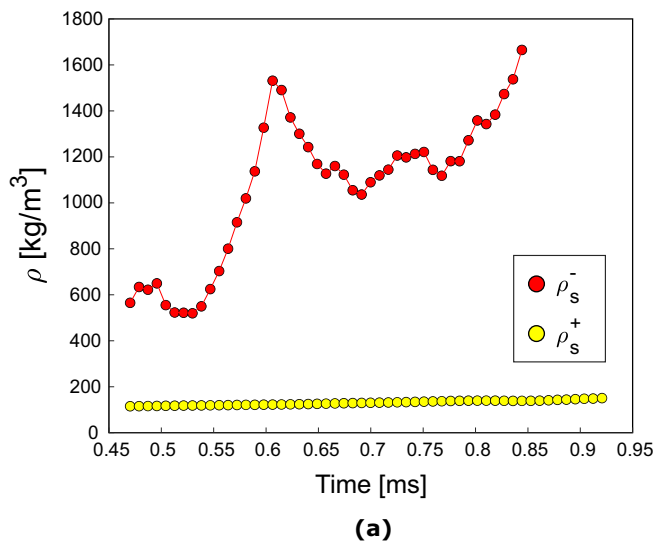

(a)

(b)

Fig. 15 Shock parameter-time histories for **a** density behind the shock, ρ_s^-, density ahead of the shock, ρ_s^+, and **b** deformed coordinate shock velocity, u_s, undeformed coordinate shock velocity, U_s, and flyer speed, $\dot{x}_{fly}$ for the Kelvin topology impacted at 67.3 m/s (Exp. #KEL_{DI3})

Figure 15b shows the corresponding undeformed coordinate shock velocity (U_s), deformed coordinate shock velocity (u_s), and flyer velocity ($\dot{x}_{fly}$) for a Kelvin specimen impacted at 67.3 m/s (Exp. #KEL_{DI3}). A large difference between the undeformed and deformed coordinate quantities reflects an effect of finite deformations ahead of the shock. These values would converge if no elastic wave or inelastic deformation ahead of the shock existed. The application of 1D shock theory may be evaluated by considering the relationship between these shock velocity quantities [52]:

$$U_s = \frac{\rho_s^-}{\rho_0}\left(u_s - \dot{x}_s^-\right) \tag{8}$$

The Lagrangian shock velocity, U_s, was found using Eq. (8) and calculated for measured quantities of ρ_s^+, $\dot{x}_s^-$, and u_s and plotted in Fig. 15b. Based upon velocities shown in Fig. 12, the particle velocity behind the shock converged to the speed of the flyer during deformation and therefore may be approximated as the flyer speed, $\dot{x}_{fly}$. Equation (8) may be considered as a mapping of the shock speed from u_s (deformed) to U_s (undeformed). Despite large differences between experimentally measured u_s and U_s values, a qualitative match was observed between the experimentally measured U_s values and the 1D shock theory-derived U_s values, which validates application of this theory.

The compaction wave speeds for each experiment are taken as the deformed coordinate shock speed, u_s, and are plotted as a function of flyer velocity in Fig. 16. Increasing compaction wave speed was observed with flyer velocity which agreed with previous studies on shock compression of foams and lattices [32, 38]. Variation in velocities existed in each experiment due to non-steady shock behavior resulting from initiation and baseplate effects. Based upon this variation, as well as non-constant densities behind the compaction wave, these results are not under the classical classification of a strong shock and are thus described as compaction waves. A general linear trend may resemble the relations shown in Fig. 16, however more data points should be collected within the steady shock regime to define a proper $u_s - u_p$ equation of state.

The stress behind the compaction wave may be found using the conservation of momentum (Eq. 5) and HPB force measurements which were used to approximate the stress state ahead of the shock, σ_s^+. Conservation of momentum may be rewritten to solve for the stress behind the shock in Eq. (9):

$$\sigma^- = \sigma^+ + u_s[\![\rho\dot{x}]\!] - [\![\rho\dot{x}^2]\!]. \tag{9}$$

Stress versus nominal impact strain histories were computed for experiments with $v_i > 45$ m/s and are shown in
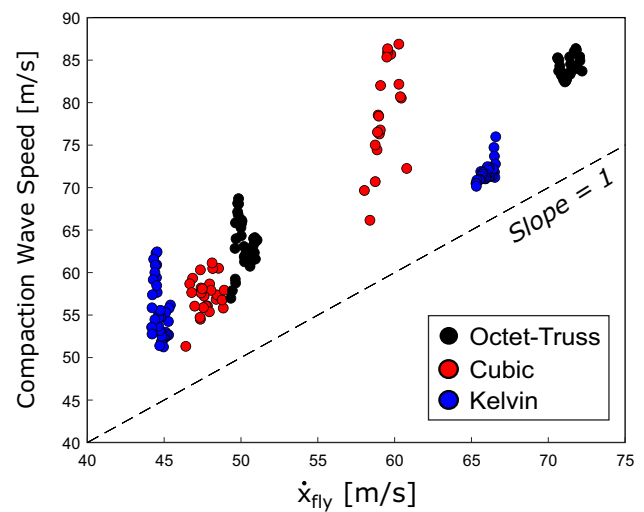

Fig. 16 Compaction wave speed (taken as deformed coordinate shock velocity (u_s)) vs. flyer velocity ($\dot{x}_{fly}$) for all topologies with impact velocity $v_i > 45$ m/s. Unit slope line drawn for reference

Fig. 17. Stress acting on the flyer was approximated by taking the product of DIC-computed accelerations and mass of the flyer. It is noted that large scatter existed in the acceleration data and smoothing was implemented in the results. There is general agreement between the 1D shock theory-calculated stress behind the compaction wave and stress acting on the flyer in terms of curve shape and magnitude, which demonstrates 1D shock theory as an appropriate technique to approximate the stress behind the compaction wave. Factors such as air resistance in the chamber or experimental DIC resolution may account for differences in measured values. The stress behind the compaction wave showed higher values than the stress state ahead of the wave, but overall curve shapes were similar. The difference between these values reflects effects of the compaction shock which are significant and caused stress enhancement by a factor of 2–3.

The stress behind the compaction wave is plotted as a function of flyer velocity in Fig. 18. A general trend of increasing stress was observed with increasing flyer velocity. The cubic topology demonstrated the highest stress values while Kelvin and octet-truss topologies showed lower values. A sharp peak in stress was observed for the cubic specimen impacted at 61.2 m/s (Exp. #CUB_{DI3}) due to the strong initial stress ahead of the shock apparent in Fig. 17 which may be related to a higher relative density of the specimen. The stress behind the shock strongly depended on the stress state ahead of the shock at these impact velocities. This in turn depends on the lattice topology and base material strain-rate dependent behavior.
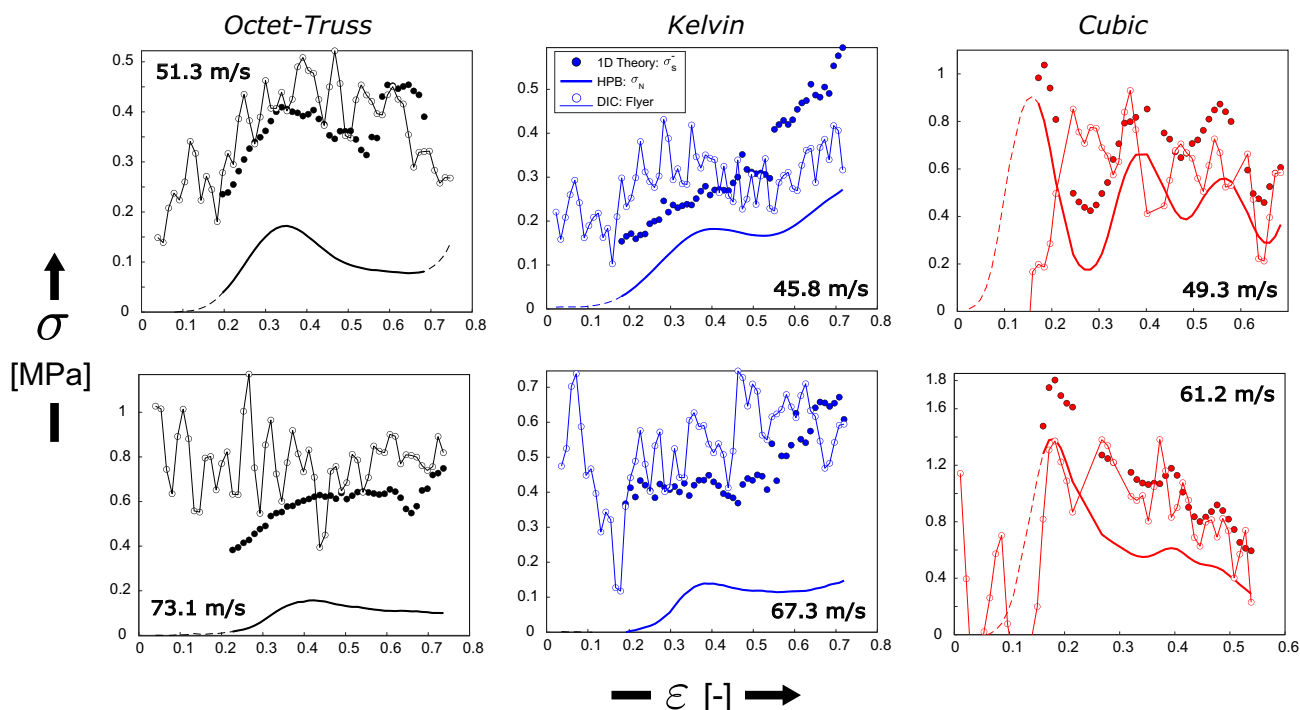
Fig. 17 Validation of 1D shock theory stress calculations from stress (σ)—nominal impact strain (ε) relations considering the stress behind the compaction wave (σ_s^-), HPB nominal stress measurements at the specimen distal face (σ_N), and DIC-computed acceleration based stresses on the flyer. Dotted lines represent HPB data outside the duration of the shock analysis
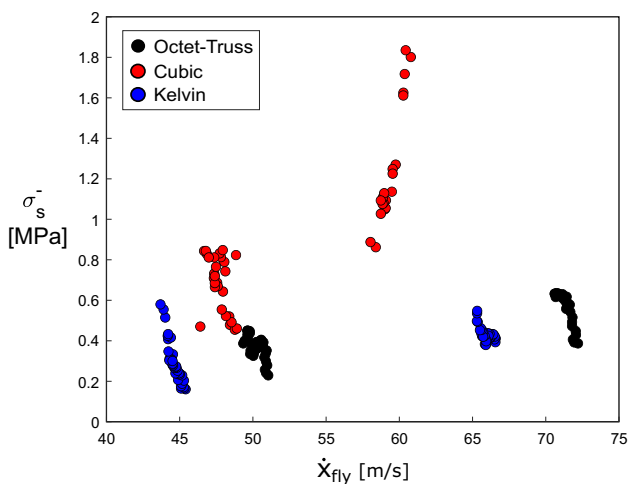

Fig. 18 Stress behind the compaction wave (σ_s^-) vs. flyer velocity ($\dot{x}_{fly}$) relation for all topologies with impact velocity $v_i > 45$ m/s

Summary and Conclusions

The transient dynamic and shock response of polymeric lattice structures of three different topologies was investigated through direct impact experiments with a polycarbonate Hopkinson pressure bar (HPB), high-speed imaging, and digital image correlation (DIC). Polymeric lattice structures with cubic, Kelvin, and octet-truss topologies were manufactured using Digital Light Processing vat polymerization and characterized at low strain-rates and impact loading. DIC was used to validate elastic HPB analysis as well as analyze the full-field mechanical response of lattice structures. Due to inhomogeneous deformation in lattices, DIC serves as a valuable tool to understand the full-field response and an excellent technique for characterization of cellular materials.

Deformation modes of lattice structures were realized in low strain-rate and impact experiments with unique behaviors demonstrated by each topology. Relevant mechanical properties of stiffness, specific energy absorption, failure stress, failure strain, and elastic wave speeds were extracted. At low to moderate impact velocities ($v_i = 25$–50 m/s), a mixed deformation mode of a compaction wave and additional deformation band formed in all topologies. At high impact velocities ($v_i > 50$ m/s), a well-defined compaction wave developed and was modeled using 1D continuum shock physics theory. Experimental shock parameters were defined to validate this theory and extract mechanical quantities such as stress behind the compaction wave.

The following conclusions are drawn from this work:

- Polymeric lattice structures demonstrate a transient dynamic deformation regime that includes a compaction

wave initiating at the impact surface and dynamic deformation in other sections of the lattice. Higher impact velocities induce a more prominent compaction response.

- Low strain-rate behavior such as stress-strain response and deformation modes (buckling in octet-truss, fracture in cubic, bending in Kelvin) match trends observed in impact experiments and may be used to estimate dynamic behavior. Low strain-rate stiffnesses and elastic wave speeds also correlate between topologies.
- Compaction wave behavior may be modeled as a compaction 'shock' in polymeric lattice structures and 1D shock theory may be used to calculate the stress at the impacted surface.
- Full-field measurements using digital image correlation allow continuous measurement of the compaction wave which permits characterization of non-steady shock propagation and geometric defects.
- Inertial effects are significant, but not fully dominant, for shock-enhanced stresses. The stress behind the compaction wave largely depends on the state ahead of the wave which demonstrates strain-rate strengthening consistent with the photopolymer base material behavior.
- Different compaction behaviors between topologies illustrate potential for engineering applications. For example, Kelvin lattices dissipated the compaction wave most while cubic lattices showed the highest impact stresses.

This work provides an experimental demonstration of a mixed deformation regime in lattice structures subject to impact loading. Additional experiments on lattices of different topologies and base materials could expand the scope of the study: impact tests with rigid anvils could be used to directly measure stress behind the compaction wave; or additional impact tests at higher velocities could be used to define the steady-state shock $u_s - u_p$ relation. Future work may also entail modeling and development of a simple theory defining lattice structure deformation across a large range of strain-rates. Low strain-rate behavior of lattices drew similarities to dynamic behavior and suggests modeling features such as general hardening, softening, or failure-based responses dependent on topology and base material.

Declarations

Conflict of interest The authors have no relevant financial or non-financial interests to disclose.

References

1. Gibson LJ, Ashby MF (1997) Cellular solids. Cambridge University Press, Cambridge. https://doi.org/10.1017/CBO9781139878326
2. Fleck NA, Deshpande VS, Ashby MF (2010) Micro-architectured materials: past, present and future. Proc R Soc A 466(2121):2495–2516. https://doi.org/10.1098/rspa.2010.0215
3. Ashby MF (2006) The properties of foams and lattices. Philos Trans R Soc A 364(1838):15–30. https://doi.org/10.1098/rsta.2005.1678
4. Zhang X, Wang Y, Ding B, Li X (2020) Design, fabrication, and mechanics of 3D micro-/nanolattices. Small 16(15):1–19. https://doi.org/10.1002/smll.201902842
5. Tofail SA, Koumoulos EP, Bandyopadhyay A, Bose S, O'Donoghue L, Charitidis C (2018) Additive manufacturing: scientific and technological challenges, market uptake and opportunities. Mater Today 21(1):22–37. https://doi.org/10.1016/j.mattod.2017.07.001
6. Helou M, Kara S (2018) Design, analysis and manufacturing of lattice structures: an overview. Int J Comput Integr Manuf 31(3):243–261. https://doi.org/10.1080/0951192X.2017.1407456
7. Tancogne-Dejean T, Li X, Diamantopoulou M, Roth CC, Mohr D (2019) High strain rate response of additively-manufactured plate-lattices: experiments and modeling. J Dyn Behav Mater 5(3):361–375. https://doi.org/10.1007/s40870-019-00219-6
8. Bonatti C, Mohr D (2019) Mechanical performance of additively-manufactured anisotropic and isotropic smooth shell-lattice materials: Simulations & experiments. J Mech Phys Solids 122:1–26. https://doi.org/10.1016/j.jmps.2018.08.022
9. Schaedler TA, Jacobsen AJ, Torrents A, Sorensen AE, Lian J, Greer JR, Valdevit L, Carter WB (2011) Ultralight metallic microlattices. Science 334(6058):962–965. https://doi.org/10.1126/science.1211649
10. Velasco-Hogan A, Xu J, Meyers MA (2018) Additive manufacturing as a method to design and optimize bioinspired structures. Adv Mater. https://doi.org/10.1002/adma.201800940
11. Xiao Z, Yang Y, Xiao R, Bai Y, Song C, Wang D (2018) Evaluation of topology-optimized lattice structures manufactured via selective laser melting. Mater Des 143:27–37. https://doi.org/10.1016/j.matdes.2018.01.023
12. Maconachie T, Leary M, Lozanovski B, Zhang X, Qian M, Faruque O, Brandt M (2019) SLM lattice structures: properties, performance, applications and challenges. Mater Design 183:108–137. https://doi.org/10.1016/j.matdes.2019.108137
13. Li X, Roth CC, Tancogne-Dejean T, Mohr D (2020) Rate- and temperature-dependent plasticity of additively manufactured stainless steel 316L: characterization, modeling and application to crushing of shell-lattices. Int J Impact Eng 145(July):103671. https://doi.org/10.1016/j.ijimpeng.2020.103671
14. Hazeli K, Babamiri BB, Indeck J, Minor A, Askari H (2019) Microstructure-topology relationship effects on the quasi-static and dynamic behavior of additively manufactured lattice structures. Mater Design 176:107826. https://doi.org/10.1016/j.matdes.2019.107826
15. Yap XY, Seetoh I, Goh WL, Ye P, Zhao Y, Du Z, Lai CQ (2021) Mechanical properties and failure behaviour of architected alumina microlattices fabricated by stereolithography 3D printing. Int

J Mech Sci 196:106285. https://doi.org/10.1016/j.ijmecsci.2021.106285

16. Bauer J, Schroer A, Schwaiger R, Kraft O (2016) Approaching theoretical strength in glassy carbon nanolattices. Nat Mater 15(4):438–443. https://doi.org/10.1038/nmat4561

17. Montemayor LC, Wong WH, Zhang YW, Greer JR (2016) Insensitivity to flaws leads to damage tolerance in brittle architected meta-materials. Sci Rep 6(February):1–9. https://doi.org/10.1038/srep20570

18. Portela CM, Edwards BW, Veysset D, Sun Y, Nelson KA, Kochmann DM, Greer JR (2021) Supersonic impact resilience of nanoarchitected carbon. Nat Mater. https://doi.org/10.1038/s41563-021-01033-z

19. Zhang Y, Yu K, Lee KH, Li K, Du H (2022) Mechanics of stretchy elastomer lattices. J Mech Phys Solids 159:104782. https://doi.org/10.1016/j.jmps.2022.104782

20. Clough EC, Plaisted TA, Eckel ZC, Cante K, Hundley JM, Schaedler TA (2019) Elastomeric microlattice impact attenuators. Matter 1(6):1519–1531. https://doi.org/10.1016/j.matt.2019.10.004

21. Tancogne-Dejean T, Spierings AB, Mohr D (2016) Additively-manufactured metallic micro-lattice materials for high specific energy absorption under static and dynamic loading. Acta Mater 116:14–28. https://doi.org/10.1016/j.actamat.2016.05.054

22. Maxwell JC (1864) L on the calculation of the equilibrium and stiffness of frames. Lond Edinburgh Dublin Philos Mag J Sci 27(182):294–299. https://doi.org/10.1080/14786446408643668

23. Calladine CR (1978) Buckminster fuller's "tensegrity'' structures and clerk Maxwell's rules for the construction of stiff frames. Int J Solids Struct 14(2):161–172. https://doi.org/10.1016/0020-7683(78)90052-5

24. Deshpande VS, Ashby MF, Fleck NA (2001) Foam topology: bending versus stretching dominated architectures. Acta Mater 49(6):1035–1040. https://doi.org/10.1016/S1359-6454(00)00379-7

25. Sun Y, Li QM (2018) Dynamic compressive behaviour of cellular materials: a review of phenomenon, mechanism and modelling. Int J Impact Eng 112:74–115. https://doi.org/10.1016/j.ijimpeng.2017.10.006

26. Xiao L, Song W (2018) Additively-manufactured functionally graded Ti–6Al–4V lattice structures with high strength under static and dynamic loading: experiments. Int J Impact Eng 111:255–272. https://doi.org/10.1016/j.ijimpeng.2017.09.018

27. Xiao L, Song W, Wang C, Tang H, Fan Q, Liu N, Wang J (2017) Mechanical properties of open-cell rhombic dodecahedron titanium alloy lattice structure manufactured using electron beam melting under dynamic loading. Int J Impact Eng 100:75–89. https://doi.org/10.1016/j.ijimpeng.2016.10.006

28. Weeks JS, Ravichandran G (2022) High strain-rate compression behavior of polymeric rod and plate Kelvin lattice structures. Mech Mater 166:104216. https://doi.org/10.1016/j.mechmat.2022.104216

29. Hawreliak JA, Lind J, Maddox B, Barham M, Messner MC, Barton NR, Jensen BJ, Kumar M (2016) Dynamic behavior of engineered lattice materials. Sci Rep 6(May):1–7. https://doi.org/10.1038/srep28094

30. Lind J, Jensen BJ, Barham MI, Kumar M (2019) In situ dynamic compression wave behavior in additively manufactured lattice materials. J Mater Res 34(1):2–19. https://doi.org/10.1557/jmr.2018.351

31. Branch BA, Specht PE, Jensen S, Jared B (2022) Detailed mesoscale simulations of the transient deformation in additively manufactured 316 L stainless steel lattices characterized by phase contrast imaging. Int J Impact Eng 161:104112. https://doi.org/10.1016/j.ijimpeng.2021.104112

32. Weeks JS, Gandhi V, Ravichandran G (2022) Shock compression behavior of stainless steel 316l octet-truss lattice structures. Int J

Impact Eng 169:104324. https://doi.org/10.1016/j.ijimpeng.2022.104324

33. Reid S, Peng C (1997) Dynamic uniaxial crushing of wood. Int J Impact Eng 19(5):531–570. https://doi.org/10.1016/S0734-743X(97)00016-X

34. Liu YD, Yu JL, Zheng ZJ, Li JR (2009) A numerical study on the rate sensitivity of cellular metals. Int J Solids Struct 46(22–23):3988–3998. https://doi.org/10.1016/j.ijsolstr.2009.07.024

35. Zou Z, Reid SR, Tan PJ, Li S, Harrigan JJ (2009) Dynamic crushing of honeycombs and features of shock fronts. Int J Impact Eng 36(1):165–176. https://doi.org/10.1016/j.ijimpeng.2007.11.008

36. Tan PJ, Reid SR, Harrigan JJ, Zou Z, Li S (2005) Dynamic compressive strength properties of aluminium foams. Part I—Experimental data and observations. J Mech Phys Solids 53(10):2174–2205. https://doi.org/10.1016/j.jmps.2005.05.007

37. Tan PJ, Reid SR, Harrigan JJ, Zou Z, Li S (2005) Dynamic compressive strength properties of aluminium foams. Part II—'shock' theory and comparison with experimental data and numerical models. J Mech Phys Solids 53(10):2206–2230. https://doi.org/10.1016/j.jmps.2005.05.003

38. Barnes AT, Ravi-Chandar K, Kyriakides S, Gaitanaros S (2014) Dynamic crushing of aluminum foams: part I—experiments. Int J Solids Struct 51(9):1631–1645. https://doi.org/10.1016/j.ijsolstr.2013.11.019

39. Sun Y, Li QM, McDonald SA, Withers PJ (2016) Determination of the constitutive relation and critical condition for the shock compression of cellular solids. Mech Mater 99:26–36. https://doi.org/10.1016/j.mechmat.2016.04.004

40. Ramesh KT (2008) high strain rate and impact mechanics. Handbook of experimental solid mechanics. pp 929–960. https://doi.org/10.1007/978-0-387-30877-7_33

41. Meyers MA (1994) Dynamic behavior of materials. Wiley, Hoboken, pp 98–123. https://doi.org/10.1002/9780470172278

42. Winter RE, Cotton M, Harris EJ, Maw JR, Chapman DJ, Eakins DE, McShane GJ (2014) Plate-impact loading of cellular structures formed by selective laser melting. Modell Simul Mater Sci Eng. https://doi.org/10.1088/0965-0393/22/2/025021

43. Luo S, Jensen B, Hooks D, Fezzaa K, Ramos K, Yeager J, Kwiatkowski K, Shimada T (2012) Gas gun shock experiments with single-pulse X-ray phase contrast imaging and diffraction at the advanced photon source. Rev Sci Instrum 83(7):073903. https://doi.org/10.1063/1.4733704

44. Schreier H, Orteu JJ, Sutton MA et al (2009) Image correlation for shape, motion and deformation measurements: basic concepts, theory and applications, vol 1. Springer, New York. https://doi.org/10.1007/978-0-387-78747-3

45. Ravindran S, Koohbor B, Malchow P, Kidane A (2018) Experimental characterization of compaction wave propagation in cellular polymers. Int J Solids Struct 139–140:270–282. https://doi.org/10.1016/j.ijsolstr.2018.02.003

46. Köhnen P, Haase C, Bültmann J, Ziegler S, Schleifenbaum JH, Bleck W (2018) Mechanical properties and deformation behavior of additively manufactured lattice structures of stainless steel. Mater Des 145:205–217. https://doi.org/10.1016/j.matdes.2018.02.062

47. Deshpande V, Fleck N, Ashby M (2001) Effective properties of the octet-truss lattice material. J Mech Phys Solids 49(8):1747–1769. https://doi.org/10.1016/S0022-5096(01)00010-2

48. Callister WD, Rethwisch DG et al (2018) Material science and engineering: an introduction, vol 9. Wiley, New York

49. Bacon C (1998) An experimental method for considering dispersion and attenuation in a viscoelastic Hopkinson bar. Exp Mech 38(4):242–249. https://doi.org/10.1177/001448519803800402

50. Messner MC, Barham MI, Kumar M, Barton NR (2015) Wave propagation in equivalent continuums representing truss lattice materials. Int J Solids Struct 73:55–66. https://doi.org/10.1016/j.ijsolstr.2015.07.023

51. Messner MC (2016) Optimal lattice-structured materials. J Mech Phys Solids 96:162–183. https://doi.org/10.1016/j.jmps.2016.07.010
52. Davison L (2008) Fundamentals of shock wave propagation in solids. Shock wave and high pressure phenomena. Springer, Berlin. https://doi.org/10.1007/978-3-540-74569-3

Publisher's Note Springer Nature remains neutral with regard to jurisdictional claims in published maps and institutional affiliations